

Stromal inflammation is a targetable driver of hematopoietic aging

Carl Mitchell

Columbia University Irving Medical Center

Evgenia Verovskaya

Columbia University Irving Medical Center

Fernando Calero-Nieto

University of Cambridge <https://orcid.org/0000-0003-3358-8253>

Oakley Olson

Columbia University Irving Medical Center

Xiaonan Wang

Cambridge Stem Cell Institute

Aurelie Herval

Genentech

Paul Dellorusso

Columbia University Irving Medical Center

James Swann

Columbia University Irving Medical Center

Si Yi Zhang

<https://orcid.org/0000-0002-5793-1151>

Arthur Svendsen

Laboratory of Ageing Biology and Stem Cells, European Research Institute for the Biology of Ageing,
University Medical Center

Eric Pietras

UCSF

Sietske Bakker

UCSF

Theodore Ho

UCSF

Berthold Gottgens

University of Cambridge <https://orcid.org/0000-0001-6302-5705>

Emmanuelle Passegué (✉ ep2828@cumc.columbia.edu)

Columbia University Medical Center <https://orcid.org/0000-0002-3516-297X>

Article

Keywords: Hematopoietic stem cells (HSC), BM niche, aging, inflammation, regeneration, IL-1, mesenchymal stromal cells (MSC), vasculature

Posted Date: November 12th, 2021

DOI: <https://doi.org/10.21203/rs.3.rs-1065222/v1>

License:  This work is licensed under a Creative Commons Attribution 4.0 International License.

[Read Full License](#)

Version of Record: A version of this preprint was published at Nature Cell Biology on January 17th, 2023. See the published version at <https://doi.org/10.1038/s41556-022-01053-0>.

Abstract

Hematopoietic aging is marked by a loss of regenerative capacity and skewed differentiation from hematopoietic stem cells (HSC) leading to impaired blood production. Signals from the bone marrow (BM) niche tailor blood production, but the contribution of the old niche to hematopoietic aging remains unclear. Here, we characterize the inflammatory milieu that drives both niche and hematopoietic remodeling. We find decreased numbers and functionality of osteoprogenitors (OPr) and expansion of pro-inflammatory perisinusoidal mesenchymal stromal cells (MSC) with deterioration of the sinusoidal vasculature, which together create a degraded and inflamed old BM niche. Niche inflammation, in turn, drives chronic activation of emergency myelopoiesis pathways in old HSCs and multipotent progenitors (MPP), which promotes myeloid differentiation at the expense of lymphoid and erythroid commitment and hinders hematopoietic regeneration. Remarkably, niche deterioration, HSC dysfunction and defective hematopoietic regeneration can all be ameliorated by blocking IL-1 signaling. Our results demonstrate that targeting IL-1 as a key mediator of niche inflammation is a tractable strategy to improve blood production during aging.

Highlights

- Both endosteal and central marrow niche populations are remodeled with age
- Old niche populations show disruption of cell identity and enrichment of inflammatory response genes
- Emergency myelopoiesis pathways are chronically activated in response to niche inflammation
- Targeting niche-mediated IL-1 signaling attenuates stromal and blood aging

Etoc Blurb

Passegué and colleagues examine the aged bone marrow niche microenvironment to understand its contribution to blood aging and identify targetable factor(s) for functional anti-aging interventions. They show that crosstalk between the inflamed niche and the inflamed hematopoietic system leads to degraded blood production both at steady state and during regeneration, and identify IL-1 as a major targetable driver of age-related niche and blood system deterioration.

Introduction

Hematopoietic function severely declines with age, causing anemia, impaired adaptive immunity, cancer and autoimmune disease in the elderly (Rossi et al., 2008). Aging also leads to major changes in bones and the bone marrow (BM) cavity, which together provide specialized niches for hematopoietic stem and

progenitor cells (HSPC) (Morrison & Scadden, 2014; Pinho & Frenette, 2019; Verovskaya et al., 2019). Blood production is tailored in part by differential production of distinct hematopoietic stem cells (HSC)-derived multipotent progenitor (MPP) subsets with specific myeloid (MPP2, MPP3) or lymphoid (MPP4) lineage biases, which in turn give rise to an array of lineage-restricted progenitors and mature cells (Pietras et al., 2015; Olson et al., 2020). Niche cells and secreted factors, in particular pro-inflammatory cytokines, play important roles in controlling blood output by regulating the number and activation state of HSCs, directing the production of progenitor cells, modulating stress hematopoiesis, and playing context-dependent roles in leukemic transformation (Morrison & Scadden, 2014; Schepers et al., 2015; Pinho & Frenette, 2019; Olson et al., 2020). Circulating levels of pro-inflammatory cytokines increase over time and contribute to the stereotypical decline in tissue integrity with age (Kovtonyuk et al., 2016; Soysal et al., 2020). By mid-life (~ 50 years in humans/~ 12 months in mice), the bones themselves are already old with thinning, impaired fracture repair, and reduced endocrine function (Almeida et al., 2013). In contrast, the most salient features of hematopoietic aging are not fully pronounced until later in life (~ 70 years in humans/~ 20-24 months in mice) and include an expansion of dysfunctional HSCs with reduced engraftment potential and impaired blood production capability (Verovskaya et al., 2019). It is now well appreciated that cell-intrinsic features such as replication stress, epigenetic remodeling and metabolic rewiring are important drivers of old HSC dysfunction, with such hardwired features not reverted by systemic rejuvenation interventions like parabiosis, plasma transfer or exercise (Ho et al., 2021). It is also clear that intrinsic changes in the BM microenvironment contribute to old HSC dysfunction (Verovskaya et al., 2019), but much less is known about the mechanisms driving niche aging and the influence of the old niche on hematopoietic aging.

The BM niche is comprised of many different cell types including mesenchymal stromal cells (MSC) and their osteoprogenitor (OPr) derivatives, endothelial cells (EC), the sympathetic nervous system, adipocytes and specific mature blood cells like megakaryocytes (Mk) and macrophages (Morrison & Scadden, 2014; Pinho & Frenette, 2019). Components of the BM microenvironment have now been extensively catalogued by imaging and molecular profiling at single cell resolution (Baryawno et al., 2019; Tikhonova et al., 2019; Baccin et al., 2020; Kokkaliaris et al., 2020). The marrow cavity is also partitioned between the endosteum lining the inner bone surface and the central marrow perivascular space, with each location exhibiting specific cellular compositions and distinct functions in regulating HSC maintenance and blood production (Morrison & Scadden, 2014; Pinho & Frenette, 2019; Verovskaya et al., 2019). Recent studies have described important age-related changes in individual niche components, particularly in the vasculature (Kusumbe et al., 2016; Poulos et al., 2017), innervation (Maryanovich et al., 2018; Ho et al., 2019) and specific stromal populations (Guidi et al., 2017; Shen et al., 2021), and reported heightened inflammation in the aged marrow cavity (Ergen et al., 2012; Ho et al., 2019; Frisch et al., 2019). However, the precise molecular underpinnings of stromal aging and whether key inflammatory mediators can be targeted to improve hematopoietic function in aging have yet to be determined. Here, we comprehensively investigate the aged BM niche microenvironment to understand its contribution to hematopoietic aging and identify targetable niche factor(s) for functional anti-aging interventions.

Results

Aging remodels the BM niche

To establish the aging features of our experimental mice, we first performed an integrated survey of bone structure and composition in cohorts of young (~ 2 months old; range of 8-12 weeks) and old (~ 24 months old; range of 22-31 months) C57BL/6 wild type (WT) mice. Hematoxylin and eosin (H&E) staining showed a fully penetrant accumulation of Mks in old mice, which was accompanied by elevated TGF- β and TPO levels in old BM fluids (**Figures S1A and S1B**) and is consistent with the known Mk bias of old HSCs (Grover et al., 2016; Poscablo et al., 2021). In contrast, we observed infrequent accumulation of adipocytes, and only in certain bones, suggesting that aging in mice is not consistently associated with increased marrow adipogenesis as in humans. Micro-computed tomography (mCT) confirmed the pronounced decay of trabecular and cortical bones in old mice (Glatt et al., 2007), which correspond to a reduction in bone-lining ALCAM⁺ osteoblasts (**Figures S1C and S1D**). These results confirm the overt stereotypical changes associated with aging in ~ 24 month-old WT mice.

We next employed a refined version of our flow cytometry-based method (Schepers et al., 2013) to investigate in the same animal both endosteal niche populations using the bone chips from 10 pooled bones (femurs, tibiae, iliac crests, humeri, ulnae and radices), and central marrow niche populations using the flushed BM plug from a single femur (**Figure 1A**; see also supplementary item **SI.1a** for gating information). Regarding the vasculature, while the overall frequency, number and preferential endosteal location of CD31^{hi}/Sca-1^{hi} arteriolar ECs (AEC) was not significantly affected with age, we observed a significant reduction in CD31^{lo}/Sca-1^{lo} sinusoidal EC (SEC) frequency and numbers both in the central marrow and at the endosteum in old mice (**Figure 1B**). This contrasts with our whole mount immunofluorescence analyses showing enhanced branching and dysmorphia of the old central marrow sinusoidal network (**Figure 1C**), and previous high-definition imaging results reporting only a specific decrease in type H transitional zone vessels (Kusumbe et al., 2016). Moreover, we confirmed unchanged vascular volume and increased vascular leakiness with age (Kusumbe et al., 2016; Poulos et al., 2017), which we found associated with decreased endocytosis of injected Dragon Green beads (DGB) in old SECs (**Figure S1E and S1F**). Accordingly, age-related changes in vascular stiffness and BM hypoxia have been shown to alter vascular integrity and contribute to degraded endothelial integrity (Xu et al., 2017). Taken together, these results indicate that SECs become dysfunctional and fragilized with age, and suggest their loss during the enzymatic digestion and cell preparation steps needed for single cell analyses, thus contributing to the observed disconnect between imaging and flow cytometry investigations.

Regarding the mesenchymal populations, old mice showed significantly decreased frequency of endosteal periarteriolar Sca-1⁺ MSCs (MSC-S) and their osteoblastic lineage cell (OLC) derivatives, which can be separated between multipotent PDGFRa⁺ OPr (mOPr) and more committed PDGFRa⁻ OPr (**Figure**

1D). Conversely, in the central marrow, we found an increase in perisinusoidal LepR⁺ MSCs (MSC-L) frequency and the striking emergence of an inflammatory Sca-1^{int} subset of MSC-L (iMSC-L) with age (**Figures 1D and 1E**). Similar iMSC-L cells were also observed following interferon exposure in polyIC-treated young mice (see supplementary item **SI.1b** for gating information), confirming the ability of some MSC-L to up-regulate Sca-1 in inflammatory contexts. Functional assessment revealed a consistent loss of fibroblastic colony-forming units (CFU-F) potential in old endosteal MSC-S and OLC populations, but not in old central marrow MSC-L (**Figure 1F**), in line with recent findings indicating that age-related impairment of osteogenesis originates at the MSC level (Ambrosi et al., 2021). Furthermore, loss and functional deterioration of endosteal mesenchymal populations were already observed in 13 month-old middle-aged mice (**Figure S1G**), directly supporting a model where niche aging precedes hematopoietic aging. Cell-intrinsic defects were also likely to be responsible for the functional decline of old MSC-S since both young and old BM cells could similarly stimulate young MSC-S colony formation, but young BM cells could not rescue the defective growth of old MSC-S in co-culture experiments (**Figure S2E**). Collectively, these results reveal a profound and complex remodeling of the old niche, with numerical loss and functional deterioration of endosteal mesenchymal populations, and expansion of inflammatory MSC-L alongside dysmorphia and fragilization of the sinusoidal network in the central marrow. They also indicate that the expanded MSC-L compartment in old mice does not functionally compensate for age-related bone loss, likely due to their known bias towards adipogenesis at the expense of osteogenesis (Nishikawa et al., 2010; Singh et al., 2016) and perhaps because of the loss of a recently described osteogenic subset of osteolectin-expressing periarteriolar MSC-L (Shen et al., 2021).

Altered signaling in old BM niche cells

To understand the molecular changes driving the remodeling of the old niche, we performed plate-based single cell RNA sequencing (scRNAseq) analyses on defined mesenchymal and endothelial populations isolated by flow cytometry from both endosteum and central marrow of young and old mice. Uniform manifold approximation and projection (UMAP) representation confirmed preservation of the overall niche structure with age (**Figure S2A**). Further visualization of mesenchymal populations highlighted the distinction between marrow MSC-L and endosteal MSC-S/mOPr/OPr, and also revealed significant contamination of old endosteal populations by expanded marrow MSC-L (**Figure 2A**). Iterative clustering and guide-gene selection (ICGS) analyses identified 16 unique cell clusters, with M1-2 associated with MSC-L identity, M3-5 with OPr identity, and M6-16 with MSC-S identity (**Figure 2B**). While most clusters had similar contribution of young and old cells, two consisted overwhelmingly of old cells (M2 and M9) while others had an under-representation of old cells (M3, M4, M12 and M15). Strikingly, M3/M4/M12/M15 all expressed genes specifically associated with osteoblastic and chondrogenic differentiation (**Table S1**), supporting a broad loss of bone-forming cells with age. In contrast, M9 was exclusively composed of old cells with downregulated bone formation pathways, while M2 was dominated by old cells with reduced expression of MSC-L identity genes and high expression of adipogenic marker genes (**Figure S2B**). In fact, a large fraction of the isolated old endosteal mOPr (45%) and OPr (58%) displayed M1 and M2 cluster identity gene expression, suggesting that they were instead

MCS-L sorted as OLC due to their reduced LepR surface expression with age (**Figure S2C**). Categorization of scRNAseq data into MSC-L-like, OPr-like and MSC-S-like identity groups showed no changes in the expression of the HSC maintenance factors *Kitl* and *Cxcl12* between young and old cells, with the numerical expansion of MSC-L likely contributing to elevated SCF levels in old BM fluids (**Figure S2D**). In contrast, gene set enrichment analysis (GSEA) of differentially expressed genes (DEG) between young and old cells within each identity group highlighted a global enrichment for inflammatory signaling pathways in all old mesenchymal populations (**Figure S2E and Table S2**). Taken together, these molecular analyses demonstrate that the age-related loss of endosteal populations and expansion of marrow MSC-L are even more pronounced than quantified by flow cytometry due to surface marker infidelity in old MSC-L. They also uncover a loss of osteoblastic/chondrogenic commitment and chronic activation of inflammatory response pathways that permeates the mesenchymal hierarchy, providing a molecular basis for the functional deterioration of old endosteal populations and associated bone loss. Moreover, they suggest that the expansion of *Kitl*-expressing MSC-L with degraded cell identity may serve to support an expanded pool of dysfunctional old HSCs.

UMAP visualization of endothelial populations clearly separated marrow ECs (mostly composed of SECs according to index sorting data) from endosteal ECs (dominated by AECs) regardless of the age of the populations (**Figure 2A**). ICGS analyses identified 7 cell clusters, with E3-4 associated with AEC identity and E7 with SEC identity (**Figure S3A and Table S1**). Ingenuity pathway analysis (IPA) of DEGs between young and old populations revealed repression of extracellular matrix genes, including many collagens, and activation of several biosynthetic pathways in old AEC-like cells (**Figures S3B and Table S2**). In contrast, old SEC-like cells showed a broad downregulation of signaling pathways, decreased expression of genes involved in endocytosis, and activation of cell death pathways. These molecular alterations likely underpin the dysfunctional and fragilized nature of old SECs, and indicate an overall loss of vascular integrity with age that also affects the arteriolar network.

Finally, we complemented our targeted single-cell niche profiling by performing unbiased droplet-based scRNAseq on unfractionated CD45⁻/Ter119⁻ endosteal and marrow stromal fractions isolated from young and old mice. UMAP representation combining both locations was indexed using a previously published taxonomy map (Baryawno et al., 2019) and annotated using projections of our plate-based scRNAseq dataset of isolated mesenchymal (MSC-L-like, OPr-like, MSC-S-like) and endothelial (SEC-like, AEC-like) populations for cluster identification (see supplementary item **SI.2** for data integration). This approach confirmed the severe degradation of the endosteal niche in old mice with reduction in MSC-S and disappearance of almost all of the OLC and OPr subsets normally found in the young niche (**Figures 2C and S3C**), directly illustrating the profound block in osteo-chondrocytic differentiation associated with aging. It also clearly captured the damaged vasculature found in old mice with a particular loss of EC subsets associated with arteriolar and sinusoidal identity. Moreover, it illustrated the major expansion of an inflammatory MSC-L1 subset of marrow MSC-L (**Figures 2C and S3C**). Collectively, these results provide a molecular roadmap of the aging BM niche and complement our flow cytometric and functional

assays in demonstrating the loss of endosteal niche populations, fragilization of the vasculature, and inflammatory remodeling of central marrow populations in old mice.

Niche-mediated inflammation in the old BM milieu

To determine how the remodeling of the old niche contributes to the establishment of an inflamed BM milieu, we used a 200-plex commercial array to screen cytokines present in BM fluids harvested from young and old mice (**Figure 3A**). Only 81 analytes were detected at both ages, with 32 upregulated and 11 downregulated with age (**Table S3**). The largest group represented inflammatory factors, some of which were previously reported to increase with age such as RANTES (Ergen et al., 2012), Eotaxin (CCL11) (Villeda et al., 2011), and IL-1 (Mrak et al., 2001; Frisch et al., 2019). The second largest group comprised soluble ligands of endothelial cells like ICAM-1 and E-selectin, whose increased levels indicate vascular activation and inflammation (Woollard et al., 2005). Other categories included cytokines and chemokines involved in bone (Abdelmagid et al., 2014) and fat (Villarroya et al., 2017) production and function, which likely reflect both the loss of OPr at the endosteum and the major expansion with age of MSC-L with known adipogenic properties (Yue et al., 2016). Complementary analyses with cytokine bead-array measurements confirmed the pro-inflammatory state of the old BM milieu, with significantly elevated levels of IL-1a/b, MIP1a, and TNFa (**Figure 3B**). Collectively, these results reveal significant changes in secreted factors in the old BM milieu and complement previous studies reporting low-grade inflammation in the aged niche (Ergen et al., 2012; Ho et al., 2019; Frisch et al., 2019).

Interestingly, while old BM fluids displayed a clear overlap with known senescence-associated secretory pathway (SASP) cytokines (Coppé et al., 2010) (**Figure S4A**), we did not find activation of senescence-related gene expression programs in any of the old mesenchymal populations (**Table S2**). Isolated old endosteal MSC-S and OLC were also negative for senescence-associated b-galactosidase (SA-b-gal) staining (**Figure S4B**). To determine whether old niche populations could directly contribute to marrow inflammation, we then screened various types of BM mature blood cells including neutrophils, macrophages, B cells and CD4⁺ T cells (see supplementary item **SI.1c** for gating information) as well as unfractionated CD45⁻/Ter-119⁻ endosteal and central marrow stromal fractions for expression of *Il1a*, *Il1b* and *Tnf* by qRT-PCR analyses (**Figure 3C**). Strikingly, only the old endosteal stromal fraction showed significantly increased *Il1b* and *Tnf* expression, with plate-based scRNAseq results confirming elevated *Il1b* levels in discrete populations of old niche cells, especially endosteal OPr and AEC as well as marrow MSC-L (**Figure 3D**). However, an increase in caspase 1 (CASP1) activity, the enzyme responsible for the intracellular processing of inactive pro-IL-1 β into mature IL-1 β , was only detectable in old mOPr with old MCS-L or BM resident macrophages, a previously identified source of IL-1b in old mice (Frisch et al., 2019), having unchanged levels of CASP1 activity compared to their young counterparts (**Figure 3E**). These results demonstrate a key role of the remodeled old niche in driving marrow inflammation, and identify the degraded endosteal OPr compartment as an important source of IL-1b production with age.

Inflammatory remodeling of the old blood system

To address the consequence of niche inflammation on the hematopoietic system, we first compared steady state hematopoiesis in young and old mice (**Figures 4A and S4C-E**; see also supplementary item **SI.1d** for gating information). Old mice displayed elevated levels of myeloid and lymphoid cells, relatively unchanged red blood cell (RBC) levels and increased platelet (Pt) counts in peripheral blood that mirror the accumulation of mature Mks and Mk progenitors (MkP) in the BM (Frisch et al., 2019; Poscablo et al., 2021). In contrast, the numbers of BM resident mature myeloid cells and committed myeloid progenitors remained fairly similar between young and old mice, while the number of common lymphoid progenitors (CLP) and B cells significantly decreased with age. Hematopoietic aging has long been characterized by an expansion of the immature Lin⁻/c-Kit⁺/Sca-1⁺ (LSK) HSPC compartment, which contains HSCs and all MPP subsets (Pietras et al., 2015). This reflected a massive expansion of CD34⁻/CD41⁺ Mk-biased HSCs that also expressed other Mk-lineage markers like P-selectin and von Willebrand Factor (vWF) (Gekas et al., 2013; Grover et al., 2016), as well as increased production of myeloid-biased MPP2 and MPP3, and decreased numbers of lymphoid-biased MPP4 (Young et al., 2016) (**Figures 4A and S4F**). To gain an unbiased view of immature HSPCs and their connection to downstream lineage-committed progenitors, we performed droplet-based scRNAseq analyses of LSK and Lin⁻/c-Kit⁺ (LK) BM fractions from young and old mice. UMAP representation combining both fractions was indexed using marker gene expression for cluster identification (Rodriguez-Fraticelli et al., 2018; Dong et al., 2020; see also supplementary item **SI.2d** for identification), although it is now well established that only a partial overlap exists between transcriptional clusters and immunophenotypically defined HSPC populations. Despite this caveat, we determined the main differentiation trajectories from HSCs, with MPP3 and MPP4 both contributing to a subset of myeloid-primed MPP(my) prior to GMP commitment, and MPP2 sitting atop the bifurcation between MkP and erythroid progenitors (EryP) (**Figures 4B and S4G**). In old mice, we also visualized and quantified the overwhelming expansion of the HSC compartment associated with MPP4 contraction and MkP expansion (**Figures 4C**). Taken together, these changes confirm well-established alterations in old HSC differentiation potential, and provide a molecular roadmap to further investigate the effect of niche inflammation on the aging blood system.

To determine the functional consequences of those changes in lineage determination in old mice, we next investigated the behavior of the old MPP populations. *In vitro*, old MPP3 showed reduced clonogenic potential in methylcellulose and accelerated myeloid differentiation in liquid culture (**Figures S5A and S5B**). In contrast, old MPP4 had elevated myeloid colony-forming activity and, similarly to MPP3 and HSCs, delayed B cell differentiation in OP9/IL-7 co-cultures (**Figure S5C**). However, none of the old MPP populations exhibited delayed division kinetics associated with replication stress (Flach et al., 2014) or dampened apoptotic responses (Gutierrez-Martinez et al., 2018) characteristic of old HSCs (**Figures S5D and S5E**). Transplantation and short-term lineage-tracking in sub-lethally irradiated recipients confirmed the reduced reconstitution activity from old MPP3, and highlighted a strong myeloid bias from every old population including MPP4 (**Figure S5F**). These results confirm altered lineage differentiation potential with age, with enhanced myeloid commitment at the expense of lymphopoiesis that is reminiscent of the engagement of emergency myelopoiesis programs (Pietras et al., 2015; Héroult et al., 2017). They also indicate that old MPPs do not share key cell-intrinsic hallmarks of HSC aging implying a role for extrinsic

niche factors in imprinting an altered behavior that persists upon the stress of *ex vivo* culture and transplantation.

To gain insight into the molecular basis of this reprogramming, we first extended our published microarray analyses of the young hematopoietic hierarchy to include old HSPCs (Pietras et al., 2015). GSEA established the unique molecular signature of old MPPs, with old MPP4 showing upregulation of cell cycle and DNA repair genes, and old MPP3 overexpression of genes associated with innate immunity and myeloid differentiation (**Figure 4D and Table S4**). Complementary Fluidigm-based qRT-PCR analyses comparing aging and our published regenerative signatures (Pietras et al., 2015) highlighted the correlation between old and 3-week post-transplantation MPP3 and MPP4, and to a lesser extent HSCs, further supporting a model whereby localized inflammation constitutively triggers normally transient myeloid regeneration programs in HSPCs (**Figure 4E**). Consistently, we also observed the presence of self-renewing GMP patches in the old BM cavity (**Figure 4F**), which were never found in young mice absent a regenerative challenge (Hérault et al., 2017). Finally, GSEA of the droplet-based scRNAseq results confirmed enhancement of myeloid/megakaryocyte and reduction of erythroid/lymphoid commitment in the old HSPC hierarchy at steady state (**Figure 4G**). They also highlighted the differential metabolic/cell cycle activation of old MPP2 (down) vs. old MPP3/MPP4 (up) and the overall increase in ribosomal protein expression with age starting in HSCs and observed throughout the HSPC hierarchy. Together, these results illustrate the profound remodeling of the hematopoietic system and blood production with age, with constitutive activation of myelopoiesis and megakaryopoiesis and suppression of lymphopoiesis and erythropoiesis. They also indicate a steady-state engagement of emergency myelopoiesis pathways in old mice characterized by HSC activation, increased production of MPP3, myeloid-reprogramming of MPP4, and GMP cluster formation, which could be directly caused by persistent exposure to niche inflammation.

Impaired hematopoietic recovery in old mice

Impaired regeneration is a defining feature of hematopoietic aging that constrains BM donor eligibility and hinders clinical chemotherapeutic usage (Verovskaya et al., 2019). To understand how the old blood system responds to hematopoietic stress, we injected young and old mice with the chemotherapeutic compound 5-fluorouracil (5FU). Old mice were exquisitely sensitive to 5FU-mediated myeloablation with ~50% mortality likely caused by massive thrombocytosis/thrombosis and anemia (**Figures 5A and 5B**). Blood analyses revealed a severely altered regenerative response with age, with a dramatic rebound and overproduction of mature myeloid cells, B cells and Pts associated with a persistent defect in erythropoiesis and loss of RBCs (**Figures 5B, 5C and 5D**). BM analyses confirmed increased myeloid cell production in response to 5FU challenge in old mice, but showed decreased B cell numbers in the marrow, suggesting that emigration rather than an increased production contributed to their elevated circulating levels. In addition, we observed an amplified HSC response associated with increased and significantly delayed MPP and myeloid progenitor activation, delayed GMP cluster differentiation, and impaired erythroid progenitor (Pre-MegE and CFU-E) production in 5FU-treated old mice (**Figures 5E and 5F**). Quantification of the local cytokine milieu indicated an exacerbation of niche inflammation in 5FU-treated

old mice, with considerably elevated IL-1a, IL-1b and MIP-1a levels in old BM fluids consistent with the role of these cytokines in promoting myelopoiesis and thrombopoiesis (**Figure 5G**) (Pietras et al., 2016; Burzynski et al., 2019). Altogether, these results suggest that by constitutively activating emergency myelopoiesis in old HSCs, age-related niche inflammation compromises acute hematopoietic regeneration and exacerbates blood aging features, ultimately furthering myeloid and platelet biases.

Chronic IL-1b exposure drives features of aging in young mice

To directly demonstrate the functional impact of age-related niche inflammation, we focused on IL-1b, an important regulator of myeloid regeneration (Olson et al., 2020), that is constitutively produced by the old endosteal niche, especially the damaged OPr compartment (**Figure 3**). Chronic IL-1b exposure in young mice is known to mimic features of blood aging (Pietras et al., 2016), with myeloid cell expansion and decreased lymphopoiesis associated with anemia and thrombocytosis (**Figure 6A**). Strikingly, we found that chronic IL-1b exposure also phenocopies several effects of aging on niche cells, with expansion of a dysmorphic and leaky sinusoidal network in the central marrow associated with SEC loss upon cell isolation, and decreased numbers of endosteal MSC-S and OLC (**Figures 6B-D**). These results indicate that elevated IL-1 levels in the aged BM directly contribute to the functional deterioration of both the niche and blood system.

Improved hematopoietic regeneration upon acute IL-1 blockade in old mice

To determine whether reducing IL-1 signaling could revert some aging features, we first administered the human IL-1 receptor antagonist Anakinra (Kineret) intraperitoneally for 14 days in young and old mice (**Figure S6A**). We used a short-term exposure paradigm to limit the risk of immune rejection, and consequently did not investigate an effect of Anakinra treatment on old BM niche cells that would have required longer treatment times to capture the slow turn-over time of stromal populations (Park et al., 2012; Schepers et al., 2013). However, we found no effects of acute inhibition of IL-1 signaling on steady state hematopoiesis, with no major changes in HSPC composition between young and old mice nor in the defective engraftment and lineage bias of old HSCs (**Figures S6B and S6C**; see also supplementary item **SI.1e** for transplantation gating information). Given the observed overproduction of IL-1a/b in old BM fluid following 5FU injection, we next investigated whether dampening IL-1 signaling to more youthful levels could improve hematopoietic regeneration upon 5FU treatment (**Figure 6E**). Strikingly, daily treatment with Anakinra from 2 days before to 12 days following 5FU injection normalized IL-1a/b levels and significantly ameliorated BM regeneration in old mice, with no visible effects on the regenerative response of young mice (**Figures 6F, 6G and S6D**). In fact, we observed a recovery from the age-associated defect in B cell and RBC production in Anakinra-treated 5FU-injected old mice, which was directly accompanied by a significant increase in MPP4 and Pre-MegE/CFU-E numbers, respectively (**Figures 6G and 6H**). IL-1b is well known to be required for effective myeloid recovery upon 5FU treatment, with *Il1r1^{-/-}* mice deficient for IL-1 signaling showing significantly impaired hematopoietic regeneration (Pietras et al., 2016). In contrast, Anakinra-mediated acute blockade of IL-1 signaling did not alter myeloid recovery in either young or old 5FU-treated mice, supporting the effectiveness of this short-

term inhibitor treatment approach, but also do not revert thrombocytosis in old mice, suggesting an improvement specific to certain blood cell lineages (**Figures 6H and S6E**). Collectively, these results demonstrate that short-term IL-1 blockade partially improves hematopoietic regeneration in old mice, with alleviation of anemia and recovery of B lymphopoiesis.

Delayed niche aging and mitigated blood aging upon long-term IL-1 inhibition

Finally, to test the necessity of IL-1 signaling in driving aging phenotypes, we analyzed young and old *Il1r1*^{-/-} mice together with age-matched *Il1r1*^{+/+} WT controls. Remarkably, old *Il1r1*^{-/-} mice displayed features of a more youthful niche, with more limited loss of endosteal mOPr and expansion of marrow MSC-L occurring without iMSC-L induction (**Figure 7A**). Molecular analyses with droplet-based scRNAseq investigations of unfractionated CD45⁻/Ter-119⁻ endosteal and marrow stromal fractions confirmed these observations and highlighted a complete rebalancing away from the inflammatory MSC-L1 subset to a more youthful MSC-L2 subset with decreased inflammatory signaling pathways and normalization of several metabolic pathways (**Figures 7B and S6F**). Old *Il1r1*^{-/-} mice also showed reduced features of blood aging both by immunophenotyping and droplet-based scRNAseq analyses of LK and LSK populations. In particular, none of the characteristic myeloid cell expansion, B cell loss and anemia were observed in the blood of old *Il1r1*^{-/-} mice, and, despite persistence of an expanded HSC compartment, an attenuation of MPP3 expansion with no increased myeloid cell production and limited loss of megakaryocyte and erythrocyte progenitors with maintenance of Pre-MegE was found in the BM of old *Il1r1*^{-/-} mice (**Figures 7C and 7D**). A more youthful rebalancing of MkP and EryP and a trend towards maintenance of the MPP4 compartment was confirmed at the molecular level (**Figures S6G and S6H**), with reversion of some GSEA lineage commitment pathways affected by aging in old *Il1r1*^{-/-} HSPCs compared to either old or young WT HSPCs, especially in the erythroid lineage (**Figures S7A and S7B**). Old *Il1r1*^{-/-} HSPCs showed recovered OXPHOS activity and dampened ribosomal protein expression that was restored to almost youthful levels as shown for *Rps29* expression (**Figures 7F and S7A**). In fact, old *Il1r1*^{-/-} HSCs exhibited increased fitness in transplantation assays, with significantly improved overall chimerism (**Figure 7G**), likely due to a rebalancing in proteostasis regulation (Kruta et al., 2021). Taken together, these results demonstrate that life-long blockade of IL-1 signaling delays stroma aging and ameliorates certain aspects of blood aging, particularly by improving circulating levels of RBC and B cells and dampening myeloid cell production. They also indicate that increased IL-1 β production by the degraded endosteal niche (mainly mOPr) acts in trans in damaging marrow MSC-L, with a combination of both direct and indirect consequences for old blood production. This conclusion is supported by *Il1r1* expression pattern, which was found strongly expressed by stromal MSC-L and BM MPP4, and much less expressed by other niche and HSPC populations (**Figure S7C**). The dominant role of IL-1 in driving age-related niche inflammation was also supported by the totally unchanged aging features observed in old *Tnf*^{-/-} mice (**Figure S7D-H**). Collectively, these results offer a proof-of-concept for blocking key niche-mediated chronic inflammatory signaling as a strategy to improve blood production and hematopoietic regeneration with age.

Discussion

Chronic inflammation is a hallmark of organismal aging, but its consequences for tissue function often remain unclear (Soysal et al., 2020). Here, we demonstrate that BM aging is defined by remodeling of the niche with increased production of pro-inflammatory cytokines by dysfunctional stromal cells and activation of immune response programs in both hematopoietic and niche cells. Such chronic, low grade “inflammaging” directly contributes to the loss of endosteal mesenchymal populations, impaired osteogenesis, and disorganization of sinusoidal blood vessels with increased vascular leakiness. These changes, alongside with an expansion of inflammatory perisinusoidal MSC-L subset, creates a self-reinforcing cycle of damage that drives lineage biases and regenerative response defects from the aged blood system. In particular, localized inflammation drives the constitutive activation of emergency myelopoiesis pathways from old HSCs and MPPs, reinforcing myeloid cell production at the expense of lymphoid and erythroid commitment. This in turn blunts regenerative responses that rely on acute activation of these pathways, leading to exacerbated phenotypes in stress conditions. Our results provide a novel understanding of blood aging based on crosstalk between the inflamed niche and inflamed hematopoietic system that degrade blood production both at steady state and during regeneration.

Previous investigations of the aged BM niche have demonstrated several complementary features to our observations. Using high-definition imaging approaches, aging has been associated with an extended sinusoidal vascular network and a specific decrease in endomucin^{bright} transitional zone (type H) vessels at the endosteum that alter bone formation through impaired Notch signaling (Kusumbe et al., 2016). The flow cytometry approach utilized in our study does not allow separation of those endothelial subsets, with *Emcn*-expressing type H vessels being captured in our broad marrow SEC-like group and their specific decrease with age overshadowed by the general loss of frail old SEC observed with digestion procedures for single cell preparation. These seemingly disparate results demonstrate the importance of using complementary investigation methods to understand different aspect of dysregulated endothelial cell biology with age. In this context, our flow cytometry investigations coupled with scRNAseq analyses also highlight a previously un-appreciated surface marker infidelity in the expanded MSC-L populations that is a central feature of the inflammatory BM niche. A reduction of endosteal niches and expansion of neurovascular central marrow niches promoting megakaryopoiesis through increased production of pro-inflammatory cytokines, including IL-6 and IL-1b, has been previously described (Ho et al., 2019). In addition, a role for IL-1b produced by aged macrophages has been directly implicated in promoting megakaryopoiesis and platelet production (Frisch et al., 2019). Here, we extend upon these findings by showing that chronic IL-1b production by the damaged endosteal niche, especially the few remaining osteoprogenitors, acts in trans by inducing inflammatory remodeling of the expanded population of perisinusoidal MSC-L and contributing to many aspects of altered blood production with age, particularly the changes in megakaryocyte/erythroid progenitor distributions and HSC activation/commitment to emergency myelopoiesis. In addition, it is likely that the indirect effect of MSC-L inflammatory remodeling

triggered by IL-1 contributes to amplify blood deregulations. However, we found that solely blocking TNF α , a potential mediator of this indirect effect (Yamashita & Passegué, 2019), does not prevent neither niche nor blood aging further highlighting the central role of IL-1 as an initiating event. In fact, blocking IL-1 signaling attenuates central marrow MSC-L niche inflammation and helps dampen HSC activation, recovering a broad range of age-related differentiation biases and improving the regeneration potential of the old blood system upon acute inhibition with Anakinra treatment.

Our findings add to the growing body of evidence for an essential role of microenvironmental inflammation in blood aging, and identify IL-1b as a key targetable driver of niche and blood system deterioration with age. This is particularly important in the context of our lack of success with attractive systemic bloodborne intervention for rejuvenating old HSC function and improving old blood production (Ho et al., 2021), likely due to their inability to alter marrow inflammation. They establish IL-1 as a central pioneering inflammaging factor that damages the crosstalk between niche and blood system, with inflammatory remodeling of the central marrow likely having deleterious consequences for niche innervation (Maryanovich et al., 2018; Ho et al., 2019) and vascular function (Kusumbe et al., 2016; Poulos et al., 2017) with age. Consistently, elevated IL-1b levels and activation of inflammasomes have been demonstrated in human studies and correlated with increased age-related mortality (Furman et al., 2017). Finally, they indicate a novel therapeutic application of IL-1 inhibitors to improve blood production in the elderly, especially when hematopoietic regeneration is needed following chemotherapy or other immunosuppressive treatments.

Limitations of the study

Our results do not formally establish the relative importance of IL-1 signaling in either stromal or hematopoietic cells in establishing phenotypes of hematopoietic aging because the lack of the IL-1 receptor or administration of Anakinra affected both compartments simultaneously in our models. Approaches such as heterochronic transplantations of young HSCs into young and old *Il1r1*^{-/-} recipients could have been used to address this question. However, our recent work showing that irradiation conditioning causes persistent changes in BM niche composition (Ho et al., 2021) raise concern about the validity of such transplantation approaches to read out stromal effect afterward. The usage of dedicated Cre driver lines, such as LepR-Cre for MSC-L, remain one of the best strategy to specifically delete *Il1r1* in defined niche populations and study its consequence over time. However, the disruptions caused by the SARS-CoV-2 pandemic precluded us to initiate these long-term studies. In spite of this, our results clearly demonstrate the importance of niche-derived IL-1 in driving inflammaging in the hematopoietic system and highlight the interconnection of the hematopoietic-stromal unit. Building on these results, our future experiments will establish the precise and combinatorial roles of other inflammatory mediators increased with age in the marrow cavity and determine whether combined interventions can further delay BM niche aging and help recover more youthful blood production.

Declarations

ACKNOWLEDGMENTS

We thank S. Villeda (UCSF) for providing some old C57Bl/6 mice, D. Reynaud (UCSF) for initial analyses of old mice, A. Valencia (UCSF) for technical assistance with various experiments, S. Kinston (Cambridge) for scRNAseq library preparations, A. Li (Bone Imaging Research Core, UCSF) for μ CT analyses, M. Lee (UCSF) and M. Kissner (CUIMC) for management of our Flow Cytometry Core facilities, and all members of the Passequé laboratory for critical insights and suggestions. C.A.M was supported by NIH F31 HL160207 and a NYSTEM training grant, E.V.V. by a Rubicon Grant from The Netherlands Organization for Scientific Research, a Stem Cell Grant from BD Biosciences, and a NYSTEM training grant, O.C.O by CRI/Margaret Dammann Eisner postdoctoral fellowship CRI3617, P.V.D by NIH F31 HL151140, J.W.S. by long-term EMBO postdoctoral fellowship ALTF-2021-196, E.M.P. by NIH F32 HL106989 and K01 DK09831, S.T.B. by a CIRM postdoctoral fellowship, and T.T.H. by an AHA and Hillblom Center for the Biology of Aging predoctoral fellowships. F.J.C-N., X.W. and B.G. were supported by grants from the Wellcome (206328/Z/17/Z), CRUK (C1163/A21762) and core funding by the Wellcome to the Cambridge Stem Cell Institute. This work was funded by NIH R01CA184014, NIH R35HL135763, Glenn Foundation Research Award and LLS Scholar Award to E.P., and supported in part through the NIH/NCI Cancer Center Support Grant P30CA013696 to CUIMC. For the purpose of Open Access, the author has applied a CC BY public copyright license to any Author Accepted Manuscript version arising from this submission.

AUTHOR CONTRIBUTIONS

E.V.V. initiated those studies and contributed to most of the experiments with help from A.H. for BMF isolation and immunophenotyping, S.Y.Z. for GMP cluster analyses and ELISA assays, A.F.S. for immunofluorescence and whole-mount staining, S.T.B for initial 5FU analyses, and T.T.H. for cell harvest and technical assistance. C.A.M. re-analyzed all the generated data, contributed to various stromal and molecular analyses and, with help from O.C.O., P.V.D and J.W.S., performed all the analyses of *Il1r1*-deficient mice. F.J.C-N., X.W. and B.G. prepared and analyzed the scRNA-seq samples, and E.M.P. prepared the microarray samples. E.V.V and E.P. designed the initial experiments, and C.A.M. and E.P. the revision experiments. Together E.V.V., C.A.M. and E.P. wrote and edited the manuscript. C.A.M. and E.P. handled the resubmission.

DECLARATION OF INTERESTS

The authors declare no competing financial interests.

References

Abdelmagid SM, Belcher JY, Moussa FM, Lababidi SL, Sondag GR, Novak KM, Sanyurah AS, Frara NA, Razmpour R, Del Carpio-Cano FE, Safadi FF. Mutation in osteoactivin decreases bone formation in vivo and osteoblast differentiation in vitro. *Am. J. Pathol.* **184**, 697-713 (2014).

- Almeida M, O'Brien CA. Basic biology of skeletal aging: role of stress response pathways. *J Gerontol A Biol Sci Med Sci* **68**, 1197-1208 (2013).
- Anders S, Pyl PT, Huber W. HTSeq—a Python framework to work with high-throughput sequencing data. *Bioinformatics* **31**, 166-169 (2015).
- Ambrosi TH, Marecic O, McArdle A, Sinha R, Gulati GS, Tong X, Wang Y, Steininger HM, Hoover MY, Koepke LS, et al. Aged skeletal stem cells generate an inflammatory degenerative niche. *Nature* **597**, 256-262 (2021).
- Baccin C, Al-Sabah J, Velten L, Helbling PM, Grünschläger F, Hernández-Malmierca P, Nombela-Arrieta C, Steinmetz LM, Trumpp A, Haas S. Combined single-cell and spatial transcriptomics reveal the molecular, cellular and spatial bone marrow niche organization. *Nat Cell Biol* **22**, 38-48 (2020).
- Bagnoli JW, Ziegenhain C, Janjic A, Wange LE, Vieth B, Parekh S, Geuder J, Hellmann I, Enard W. Sensitive and powerful single-cell RNA sequencing using mcSCR-seq. *Nat Commun* **9**, 2937 (2018).
- Baryawno N, Przybylski D, Kowalczyk MS, Kfoury Y, Severe N, Gustafsson K, Kokkaliaris KD, Mercier F, Tabaka M, Hofree M, et al. A cellular taxonomy of the bone marrow stroma in homeostasis and leukemia. *Cell* **177**, 1915-1932 (2019).
- Brennecke P, Anders S, Kim JK, Kołodziejczyk AA, Zhang X, Proserpio V, Baying B, Benes V, Teichmann SA, Marioni JC, Heisler MG. Accounting for technical noise in single-cell RNA-seq experiments. *Nat Methods* **10**, 1093-1095 (2013).
- Burzynski LC, Humphry M, Pyrillou K, Wiggins KA, Chan JNE, Figg N, Kitt LL, Summers C, Tatham KC, Martin PB, et al. The coagulation and immune systems are directly linked through the activation of interleukin-1 α by thrombin. *Immunity* **50**, 1033-1042 (2019).
- Coppé JP, Desprez PY, Krtolica A, Campisi J. The senescence-associated secretory phenotype: the dark side of tumor suppression. *Annu Rev Pathol* **5**, 99-118 (2010).
- Dong F, Hao S, Zhang S, Zhu C, Cheng H, Yang Z, Hamey FK, Wang X, Gao A, Wang F, Gao Y, Dong J, Wang C, Wang J, Lan Y, Liu B, Ema H, Tang F, Göttgens B, Zhu P, Cheng T. Differentiation of transplanted haematopoietic stem cells tracked by single-cell transcriptomic analysis. *Nat Cell Biol* **22**, 630-639 (2020).
- Ergen AV, Boles NC, Goodell MA. Rantes/Ccl5 influences hematopoietic stem cell subtypes and causes myeloid skewing. *Blood* **119**, 2500-2509 (2012).
- Flach J, Bakker ST, Mohrin M, Conroy PC, Pietras EM, Reynaud D, Alvarez S, Diolaiti ME, Ugarte F, Forsberg EC, et al. Replication stress is a potent driver of functional decline in ageing haematopoietic stem cells. *Nature* **512**, 198-202 (2014).

Frisch BJ, Hoffman CM, Latchney SE, LaMere MW, Myers J, Ashton J, Li AJ, Saunders J 2nd, Palis J, Perkins AS, et al. Aged marrow macrophages expand platelet-biased hematopoietic stem cells via Interleukin1B. *JCI Insight* **5**, e124213 (2019).

Furman D, Chang J, Lartigue L, Bolen CR, Haddad F, Gaudilliere B, Ganio EA, Fragiadakis GK, Spitzer MH, Douchet I, et al. Expression of specific inflammasome gene modules stratifies older individuals into two extreme clinical and immunological states. *Nat Med* **23**, 174-184 (2017).

Gekas C, Graf T. CD41 expression marks myeloid-biased adult hematopoietic stem cells and increases with age. *Blood* **121**, 4463-4472 (2013).

Glatt V, Canalis E, Stadmeier L, Bouxsein ML. Age-related changes in trabecular architecture differ in female and male C57BL/6J mice. *J Bone Miner Res* **22**, 1197–1207 (2007).

Grover A, Sanjuan-Pla A, Thongjuea S, Carrelha J, Giustacchini A, Gambardella A, Macaulay I, Mancini E, Luis TC, Mead A, et al. Single-cell RNA sequencing reveals molecular and functional platelet bias of aged haematopoietic stem cells. *Nat Commun* **7**:11075 (2016).

Guidi N, Sacma M, Ständker L, Soller K, Marka G, Eiwen K, Weiss JM, Kirchhoff F, Weil T, Cancelas JA, et al. Osteopontin attenuates aging-associated phenotypes of hematopoietic stem cells. *EMBO J* **36**, 1463 (2017).

Gutierrez-Martinez P, Hogdal L, Nagai M, Kruta M, Singh R, Sarosiek K, Nussenzweig A, Beerman I, Letai A, Rossi DJ. Diminished apoptotic priming and ATM signalling confer a survival advantage onto aged haematopoietic stem cells in response to DNA damage. *Nat Cell Biol* **20**, 413-421 (2018).

Hao Y, Hao S, Andersen-Nissen E, Mauck WM 3rd, Zheng S, Butler A, Lee MJ, Wilk AJ, Darby C, Zager M, et al. Integrated analysis of multimodal single-cell data. *Cell* **184**, 3573-3587 (2021).

Hérault A, Binnewies M, Leong S, Calero-Nieto FJ, Zhang SY, Kang YA, Wang X, Pietras EM, Chu SH, Barry-Holson K, et al. Myeloid progenitor cluster formation drives emergency and leukemic myelopoiesis. *Nature* **544**, 53-58 (2017).

Ho YH, Del Toro R, Rivera-Torres J, Rak J, Korn C, García-García A, Macías D, González-Gómez C, Del Monte A, Wittner M, et al. Remodeling of bone marrow hematopoietic stem cell niches promotes myeloid cell expansion during premature or physiological aging. *Cell Stem Cell* **25**, 407-418 (2019).

Ho TT, Dellorusso PV, Verovskaya EV, Bakker ST, Flach J, Smith LK, Ventura PB, Lansinger OM, Hérault A, Zhang SY, et al. Aged hematopoietic stem cells are refractory to bloodborne systemic rejuvenation interventions. *J Exp Med* **218**, e20210223 (2021).

Kokkaliaris K, Kunz L, Cabezas-Wallscheid N, Christodoulou C, Renders S, Camargo F, Trumpp A, Scadden DT, Schroeder T. Adult blood stem cell localization reflects the abundance of reported bone marrow niche cell types and their combinations. *Blood* **136**, 2296-2307 (2020).

Kovtonyuk LV, Fritsch K, Feng X, Manz MG, Takizawa H. Inflamm-aging of hematopoiesis, hematopoietic stem cells, and the bone marrow microenvironment. *Front Immunol* **7**, 502 (2016).

Kruta M, Sunshine MJ, Chua BA, Fu Y, Chawla A, Dillingham CH, Hidalgo San Jose L, De Jong B, Zhou FJ, Signer RAJ. Hsf1 promotes hematopoietic stem cell fitness and proteostasis in response to ex vivo culture stress and aging. *Cell Stem Cell* **online ahead of print**, S1934-5909(21)00294-0 (2021)

Kusumbe AP, Ramasamy SK, Itkin T, Mäe MA, Langen UH, Betsholtz C, Lapidot T, Adams RH. Age-dependent modulation of vascular niches for haematopoietic stem cells. *Nature* **532**, 380-384 (2016).

Love MI, Huber W, Anders S. Moderated estimation of fold change and dispersion for RNA-seq data with DESeq2. *Genome Biol.* **15**, 55 (2014).

Maryanovich M, Ramalingam P, Gutkin MC, Llanos P, Gilleran K, Rabbany SY, Butler JM. Adrenergic nerve degeneration in bone marrow drives aging of the hematopoietic stem cell niche. *Nat Med* **24**, 782-791 (2018).

Morrison SJ, Scadden DT. The bone marrow niche for haematopoietic stem cells. *Nature* **505**, 327-334 (2014).

Mrak RE, Griffin WS. Interleukin-1, neuroinflammation, and Alzheimer's disease. *Neurobiol Aging* **22**, 903-908 (2001).

Nishikawa K, Nakashima T, Takeda S, Isogai M, Hamada M, Kimura A, Kodama T, Yamaguchi A, Owen MJ, Takahashi S, Takayanagi H. Maf promotes osteoblast differentiation in mice by mediating the age-related switch in mesenchymal cell differentiation. *J Clin Invest* **120**:3455-3465 (2010).

Olson OC, Kang Y-A, Passegué E. Normal Hematopoiesis Is a Balancing Act of Self-Renewal and Regeneration. In *Cold Spring Harb Perspect Med*, Jan 27:a035519 (2020).

Olsson A, Venkatasubramanian M, Chaudhri VK, Aronow BJ, Salomonis N, Singh H, Grimes HL. Single-cell analysis of mixed-lineage states leading to a binary cell fate choice. *Nature* **537**, 698-702 (2016).

Park D, Spencer JA, Koh BI, Kobayashi T, Fujisaki J, Clemens TL, Lin CP, Kronenberg HM, Scadden DT. Endogenous bone marrow MSCs are dynamic, fate-restricted participants in bone maintenance and regeneration. *Cell Stem Cell* **10**, 259-72 (2012).

Picelli S, Faridani OR, Björklund AK, Winberg G, Sagasser S, Sandberg R. Full-length RNA-seq from single cells using Smart-seq2. *Nat Protoc* **9**, 171-181 (2014).

Pietras EM, Reynaud D, Kang YA, Carlin D, Calero-Nieto FJ, Leavitt AD, Stuart JM, Göttgens B, Passegué E. Functionally distinct subsets of lineage-biased multipotent progenitors control blood production in normal and regenerative conditions. *Cell Stem Cell* **17**, 35-46 (2015).

- Pietras EM, Mirantes-Barbeito C, Fong S, Loeffler D, Kovtonyuk LV, Zhang S, Lakshminarasimhan R, Chin CP, Techner JM, Will B, et al. Chronic interleukin-1 exposure drives haematopoietic stem cells towards precocious myeloid differentiation at the expense of self-renewal. *Nat Cell Biol* **18**, 607-618 (2016).
- Pinho S, Frenette PS. Haematopoietic stem cell activity and interactions with the niche. *Nat Rev Mol Cell Biol* **20**, 303-320 (2019).
- Poscablo DM, Worthington AK, Smith-Berdan S, Forsberg EC. Megakaryocyte progenitor cell function is enhanced upon aging despite the functional decline of aged hematopoietic stem cells. *Stem Cell Reports* **16**, 1598-1613 (2021).
- Poulos, M.G., et al. Endothelial transplantation rejuvenates aged hematopoietic stem cell function. *J Clin Invest* **127**, 4163-4178 (2017).
- Rossi DJ, Jamieson CHM, Weissman IL. Stems cells and the pathways to aging and cancer. *Cell* **132**, 681-696 (2008).
- Rodriguez-Fraticelli AE, Wolock SL, Weinreb CS, Panero R, Patel SH, Jankovic M, Sun J, Calogero RA, Klein AM, Camargo FD. Clonal analysis of lineage fate in native haematopoiesis. *Nature* **553**, 212-216 (2018).
- Schepers K, Pietras EM, Reynaud D, Flach J, Binnewies M, Garg T, Wagers AJ, Hsiao EC, Passegué E. Myeloproliferative neoplasia remodels the endosteal bone marrow niche into a self-reinforcing leukemic niche. *Cell Stem Cell* **13**, 285-299 (2013).
- Schepers K, Campbell TB, Passegué E. Normal and Leukemic Stem Cell Niches: Insights and Therapeutic Opportunities. *Cell Stem Cell* **16**, 254-267 (2015).
- Shen B, Tasdogan A, Ubellacker JM, Zhang J, Nosyreva ED, Du L, Murphy MM, Hu S, Yi Y, Kara N, et al. A mechanosensitive peri-arteriolar niche for osteogenesis and lymphopoiesis. *Nature* **591**, 438-444. (2021).
- Singh L, Brennan TA, Russell E, Kim JH, Chen Q, Brad Johnson F, Pignolo RJ. Aging alters bone-fat reciprocity by shifting in vivo mesenchymal precursor cell fate towards an adipogenic lineage. *Bone* **85**:29-36 (2016).
- Soysal P, Arik F, Smith L, Jackson SE, Isik AT. Inflammation, frailty and cardiovascular disease. *Adv Exp Med Biol* **1216**, 55-64 (2020).
- Stuart T, Butler A, Hoffman P, Hafemeister C, Papalexi E, Mauck WM, Hao Y, Stoeckius M, Smibert P, Satija R. Comprehensive Integration of Single Cell Data. *Cell* **177**, 1888-1902 (2019).
- Tikhonova AN, Dolgalev I, Hu H, Sivaraj KK, Hoxha E, Cuesta-Domínguez Á, Pinho S, Akhmetzyanova I, Gao J, Witkowski M, et al. The bone marrow microenvironment at single-cell resolution. *Nature* **569**, 222-228 (2019).

Tusher VG, Tibshirani R, Chu G. Significance analysis of microarrays applied to the ionizing radiation response. *Proc Natl Acad Sci USA* **98**, 5116-5121 (2001).

Valletta S, Thomas A, Meng Y, Ren X, Drissen R, Sengül H, Di Genua C, Nerlov C. Micro-environmental sensing by bone marrow stroma identifies IL-6 and TGF β 1 as regulators of hematopoietic ageing. *Nat Commun* **11**, 4075 (2020).

Verovskaya EV, Dellorusso PV, Passequé E. Losing sense of self and surroundings: hematopoietic stem cell aging and leukemic transformation. *Trends Mol Med* **25**, 494-515 (2019).

Villarroya F, Cereijo R, Villarroya J, Giral M. Brown adipose tissue as a secretory organ. *Nat. Rev. Endocrinol.* **13**, 26-35 (2017).

Villeda SA, Luo J, Mosher KI, Zou B, Britschgi M, Bieri G, Stan TM, Fainberg N, Ding Z, Eggel A, et al. The ageing systemic milieu negatively regulates neurogenesis and cognitive function. *Nature* **477**, 90-94 (2011).

Wolf FA, Angerer P, Theis FJ. SCANPY: large-scale single-cell gene expression data analysis. *Genome Biol* **19**, 15 (2018).

Wolock SL, Lopez R, Klein AM. Scrublet: computational identification of cell doublets in single-cell transcriptomic data. *Cell Syst* **8**, 281-291 (2019).

Woollard KJ. Soluble bio-markers in vascular disease: much more than gauges of disease? *Clin Exp Pharmacol Physiol* **32**, 233-240 (2005).

Xu X, Wang B, Ren C, Hu J, Greenberg DA, Chen T, Xie L, Jin K. Age-related impairment of vascular structure and functions. *Aging Dis* **8**, 590-610 (2017).

Yamashita M, Passequé E. TNF- α coordinates hematopoietic stem cell survival and myeloid regeneration. *Cell Stem Cell* **25**, 357-372 (2019).

Young K, Borikar S, Bell R, Kuffler L, Philip V, Trowbridge JJ. Progressive alterations in multipotent hematopoietic progenitors underlie lymphoid cell loss in aging. *J Exp Med* **213**, 2259-2267 (2016).

Yue R, Zhou BO, Shimada IS, Zhao Z, Morrison SJ. Leptin receptor promotes adipogenesis and reduces osteogenesis by regulating mesenchymal stromal cells in adult bone marrow. *Cell Stem Cell* **18**, 782-796 (2016).

Zhou BO, Yue R, Murphy MM, Peyer JG, Morrison SJ. Leptin-receptor-expressing mesenchymal stromal cells represent the main source of bone formed by adult bone marrow. *Cell Stem Cell* **15**, 154-168 (2014).

Star Methods

Contact for Reagent and Resource Sharing

Further information and requests for resources and reagents should be directed to and will be fulfilled by the Lead Contact, Emmanuelle Passegué, ep2828@cumc.columbia.edu.

Experimental Model and Subject Details

Mice

Young and old wild-type C57BL/6-CD45.2 (B6) and wild-type C57BL/6-CD45.1 (BoyJ) mice of both sexes were bred and aged in house either at UCSF or CUIMC. Some old B6 mice were also obtained from the National Institute on Aging (NIA) aged rodent colonies and from collaborators. β -actin-GFP C57BL/6-CD45.2 transgenic mice (Pietras et al., 2015), $Il1r1^{-/-}$ C57BL/6-CD45.2 mice (Pietras et al., 2016) and $Tnf^{-/-}$ C57BL/6-CD45.2 mice (Yamashita & Passegué, 2019) were previously described. At the time of analyses, young mice were 6-12 weeks of age, middle-age mice were 13 months old, and old mice were all ≥ 22 months of age, most of them ~ 24 month of age with some reaching 31 months of age. Young BoyJ recipient mice for HSC and MPP primary and secondary transplantation assays were 8-12 weeks of age at time of irradiation. No specific randomization or blinding protocol was used with respect to the identity of experimental animals, and both male and female animals were used indiscriminately in all experiments. All mice were maintained in mouse facilities at UCSF or CUIMC in accordance with IACUC protocols approved at each institution.

Method Details

In vivo assays

For quantitative Dragon Green Bead (DGB; Bangs Laboratories, FSDG001) analyses, mice were injected retro-orbitally with 2.5 μ l/g DGB solution under isoflurane anesthesia 10 min prior to euthanasia by CO₂ asphyxiation and immediately perfused with 20 ml PBS by cardiac puncture before bone harvest. For 5-fluorouracil (5FU; Sigma-Aldrich) treatment, mice were injected intraperitoneally with 150 mg/kg 5FU or vehicle (PBS) and analyzed for blood and BM parameters. For chronic IL-1 treatment, mice were injected intraperitoneally with 0.5 μ g IL-1 β (Peprotech, 211-11B) in 100 μ l PBS/0.2% BSA or vehicle (PBS/0.2% BSA) daily for 20 days and analyzed for blood and BM parameters. For Anakinra treatment, mice were injected intraperitoneally with 10 mg/kg Anakinra (Swedish Orphan Biovitrum AB, 666-58234-07) or vehicle (PBS) daily for 14 days, with or without 5FU injection on the third day, and analyzed for blood and BM parameters. For transplantation experiments, CD45.1 recipient mice were exposed to 9 Gy (sub-lethal) or 11 Gy (lethal) irradiation dose delivered in split doses 3 hours apart using either a ¹³⁷Cs source (J. L. Shepherd) or an X-ray irradiator (MultiRad225, Precision X-Ray Irradiation), and purified HSCs and MPPs were delivered via retro-orbital injection. For transplantation into sub-lethally-irradiated recipients, mice were injected with 2,000-5,000 purified CD45.2 HSCs or MPPs. For transplantation in lethally-irradiated recipients, mice were injected with 250 CD45.2 HSCs delivered together with 300,000 Sca-1-depleted CD45.1 helper BM cells. Recipient mice were administered polymyxin/neomycin-containing water for 4

weeks following the procedure to prevent opportunistic infection, and analyzed for blood and BM parameters. Peripheral blood was collected under isoflurane anesthesia via retro-orbital bleeding and dispensed into EDTA-coated tubes (Becton Dickinson) for complete blood count (CBC) analyses using a Genesis (Oxford Science) hematology system. BM analyses were terminal analyses at the time of tissue harvest and BM cellularity was determined using a ViCell automated cell counter (Beckman-Coulter).

Flow cytometry of hematopoietic cells

BM hematopoietic stem, progenitor and mature cell populations were analyzed and/or purified as previously described (Pietras et al., 2015). In brief, BM cells were obtained by crushing leg, arm, and pelvic bones (with sternum and spines for some experiments) in staining media composed of Hanks' buffered saline solution (HBSS) containing 2% heat-inactivated FBS (Cellgro B003L52). Red blood cells were removed by lysis with ACK (150 mM NH₄Cl/10 mM KHCO₃) buffer, and single-cell suspensions of BM cells were purified on a Ficoll gradient (Histopaque 1119, Sigma-Aldrich). For HSC and progenitor isolation, BM cells were pre-enriched for c-Kit⁺ cells using c-Kit microbeads (Miltenyi Biotec, 130-091-224) and an AutoMACS cell separator (Miltenyi Biotec). Unfractionated or c-Kit-enriched BM cells were then incubated with purified rat anti-mouse lineage antibodies (CD3, BioLegend, 100202; CD4, eBioscience, 16-0041-82; CD5, BioLegend, 100602; CD8, BioLegend, 100702; CD11b, BioLegend, 101202; B220, BioLegend, 103202; Gr1, eBioscience, 14-5931-85; Ter119, BioLegend, 116202) followed by goat anti-rat-PE-Cy5 (Invitrogen, A10691) and subsequently blocked with purified rat IgG (Sigma-Aldrich). Cells were then stained with c-Kit-APC-Cy7 (BioLegend, 105826), Sca-1-PB (BioLegend, 108120) or Sca-1-BV421 (BioLegend, 108128), CD150-PE (BioLegend, 115904) or CD150-BV650 (BioLegend, 115931), CD48-A647 (BioLegend, 115904) or CD48-A700 (BioLegend, 103426), and Flk2-biotin (eBioscience, 13-1351-85) or Flk2-PE (eBioscience, 12-1351-82) followed by SA-PE-Cy7 (eBioscience, 25-4317-82) for HSC/MPP staining, or together with CD34-FITC (eBioscience, 11-0341-85) or CD34-biotin (BioLegend, 119304) and FcγR-PerCP-Cy5.5 (eBioscience, 46-0161-82) or FcγR-PE-Cy7 (BioLegend, 101317) followed by SA-BV605 (BioLegend, 405229) for combined HSC/MPP/myeloid progenitor staining. For quantification of HSC surface marker expression, CD41-FITC (eBioscience, 11-0411-82), CD62P-FITC (BD, 561923) and vWF-FITC (EMFRET, P150-1) were also used. For extended myeloerythroid progenitor staining, unfractionated BM cells were incubated with Lin/PE-Cy5 and then CD41-PE (BD, 558040) or CD41-BV510 (BioLegend, 133923), FcγR-PerCP-Cy5.5 or FcγR-PE-Cy7, CD150-APC (BioLegend, 115910) or CD150-BV650, and CD105-A488 (BioLegend, 120406) or CD105-BV605 (BD, 740425). For CLP staining, unfractionated BM cells were incubated with Lin/PE-Cy5, then cKit-APC-Cy7, Sca-1-PB, Flk2-biotin, and IL7R-PE (eBioscience, 12-1271-82) followed by SA-PE-Cy7. For mature cell analyses, depending on the experiments, BM cells were stained with Mac-1-PE-Cy7 (eBioscience, 25-0112-82), Gr-1-e450 (eBioscience, 57-5931-82), B220-APC-Cy7 (eBioscience, 47-0452-82), and CD3-FITC (BioLegend, 100306). For myeloid cell isolation for qRT-PCR analyses, BM cells were stained with CD3-PE-Cy5 (eBioscience, 15-0031-63), B220-PE-Cy5 (eBioscience, 15-0452-82), NK1.1-PE-Cy5 (BioLegend, 108716), CD11b-FITC (eBioscience, 11-0112-82), Ly-6C-APC-Cy7 (BioLegend, 128025) and Ly-6G-A700 (BioLegend, 127622). For lymphoid cell isolation for qRT-PCR analyses, BM cells were stained with B220-APC-Cy7, CD19-PE (eBioscience, 12-0193-82), TCRβ-

PE-Cy7 (Invitrogen, 25-5961-80), CD4-PE-Cy5 (eBioscience, 15-0041-82), and CD8-A700 (Pharmingen, 557959). For *in vitro* differentiation assays, cultured cells were stained with c-Kit-APC-Cy7, Sca-1-PB, Mac-1-PE-Cy7 and FcγR-PE (eBioscience, 12-0161-83) for myeloid differentiation, or Mac-1-APC (eBioscience, 17-0112-82) and CD19-PB (BioLegend, 115523) for lymphoid differentiation on OP9 cells. For HSC chimerism analyses, HSCs were stained with Lin/PE-Cy5, c-Kit-APC-Cy7, Sca-1-BV421, CD150-BV650, CD48-A700, and Flk2-bio followed by SA-BV605, together with CD45.2-FITC (eBioscience, 11-0454-85) and CD45.1-PE (eBioscience, 25-0453-83). For peripheral blood chimerism analyses, cells were stained with Mac-1-PE-Cy7, Gr-1-e450, B220-APC-Cy7, CD3-APC (eBioscience, 17-0032-82), and Ter-119-PE-Cy5 (eBioscience, 15-5921-83) together with CD45.2-FITC and CD45.1-PE. Before isolation or analyses, stained cells were resuspended in staining media containing 1 µg/ml propidium iodide (PI) for dead cell exclusion. HSC and progenitor cell isolations were performed on a Becton Dickinson (BD) FACS Aria II (UCSF) or FACS Aria II SORP (CUIMC) using double sorting for purity. Mature cell isolations were performed on a FACS Aria II SORP using single sorting on purity mode. Cell analyses were performed either on the same FACS ARIA, or on a BD LSR II (UCSF), BD Celesta (CUIMC), Bio-Rad ZE5 (CUIMC) or Novacyte Quanteon (CUIMC) cell analyzer. For all experiments, HSCs were identified as Lin⁻/Sca-1⁺/c-Kit⁺/Flk2⁻/CD48⁻/CD150⁺ BM cells, MPP3 as Lin⁻/Sca-1⁺/c-Kit⁺/Flk2⁻/CD48⁺/CD150⁺ BM cells, MPP4 as Lin⁻/Sca-1⁺/c-Kit⁺/Flk2⁺ BM cells, and, except when indicated, granulocytes (Gr) cells as Mac-1⁺/Gr-1⁺ BM cells, B cells as B220⁺ BM cells and T cells as CD3⁺ BM cells.

Flow cytometry of niche cells

Endosteal stromal cells were isolated as previously described (Schepers et al., 2013). In brief, leg, arm, and pelvic bones were gently crushed and washed with HBSS until white. Stromal cells were released by treatment with 3 mg/ml Type I Collagenase (Worthington) in 2 ml HBSS for 1 hr at 37°C with shaking at 110 rpm. Stromal cells were washed with HBSS + 4% FBS and filtered through 45 µm mesh into a polypropylene tube. Isolation of central marrow stromal cells was adapted from a published protocol (Zhou et al., 2014) using individual femurs with the femoral head cut off and kneecap removed to expose the growth plate. Intact BM plugs were carefully flushed with HBSS into polypropylene tubes by inserting 1 ml syringes with 22G needles into the growth plate. HBSS was discarded and stromal cells were released by digestion with 3 mg/ml Type I Collagenase (Worthington) in 1 ml HBSS for 10 min twice at 37°C with shaking at 110 rpm. After the second incubation the plugs were resuspended by pipetting and filtered through 45 µm mesh into a new tube. Both endosteal and central marrow stromal cells were stained with Ter119-PE-Cy5, CD45-APC-Cy7 (BD, 557659), CD31-PE (BD, 553373), Sca-1-A700 (eBioscience, 56-5981-82), CD105-BV786 (BD, 564746), CD51-BV421 (BD, 740062), PDGFRa-PE-Cy7 (eBioscience, 25-1401-82) and LepR-biotin (R&D Systems, BAF497) followed by SA-APC (eBioscience, 17-4317-82), and resuspended in HBSS with 4% FBS and PI. Both cell isolations and analyses were performed on a Becton Dickinson (BD) FACS Aria II (UCSF) or FACS Aria II SORP (CUIMC) using single sorting on purity mode. For all experiments, MSC-S were identified as Ter119⁻/CD45⁻/CD31⁻/Sca-1⁺/CD51⁺, OLC as Ter119⁻/CD45⁻/CD31⁻/Sca-1⁻/CD51⁺, mOPr as Ter119⁻/CD45⁻/CD31⁻/Sca-1⁻/CD51⁺/PDGFRa⁺/LepR⁻, OPr as Ter119⁻/CD45⁻/CD31⁻/Sca-1⁻/CD51⁺/PDGFRa⁻/LepR⁻ and AEC

as Ter119⁻/CD45⁻/CD31⁺/Sca-1^{hi}/CD105^{lo} endosteal cells, while MSC-L were identified as Ter119⁻/CD45⁻/CD31⁻/Sca-1⁻/CD51⁺/PDGFRa⁺/LepR⁺ and SEC as Ter119⁻/CD45⁻/CD31⁺/Sca-1^{lo}/CD105^{hi} central marrow cells.

In vitro assays

All cultures were performed at 37 °C in a 5% CO₂ water jacket incubator (ThermoFisher). For methylcellulose colony assays, single cells were directly sorted into individual wells of a flat-bottom 96-well plate (Fisher Scientific, 353072) containing 100 µl methylcellulose (Stem Cell Technologies, M3231) supplemented with penicillin (50 U/ml)/streptomycin (50 µg/ml), 0.1 mM non-essential amino acids (Fisher Scientific, 11-140-050), 1 mM sodium pyruvate (Fisher Scientific, 11-360-070), 2 mM L-glutamine (Fisher Scientific 35-050-061), 50 µM 2-mercaptoethanol (Sigma, M7522) and the following cytokines (all from PeproTech): IL-3 (10 ng/ml), GM-CSF (10 ng/ml), SCF (25 ng/ml), IL-11 (25 ng/ml), Flt-3L (25 ng/ml), TPO (25 ng/ml) and EPO (4 U/ml). Colonies were visually scored after 7 days of culture. For myeloid differentiation assays, 1,000 cells were directly sorted into individual wells of a 96-well plate containing Iscove's modified Dulbecco's media (IMDM) medium (Invitrogen) supplemented with 5% FBS (StemCell Technology, 06200) and the same reagents and cytokine cocktail than the methylcellulose assays (full cytokine medium). Cells were analyzed by flow cytometry after different culture periods. For cleaved caspase 3/7 (CC3/7) assays, 400-600 cells were directly sorted in triplicate into 40 µl full cytokine medium in a 384-well plate, and incubated for 24 hr before adding 40 µl of Caspase-Glo 3/7 (Promega) to each well. Plates were then shaken for 30 s at 500 rpm, incubated for 45 min at RT and read on a luminometer (Synergy2, BioTek) to obtain relative units (RU). OP9 stromal cells (ATCC, CRL-2749) were maintained in Minimum Essential Medium Eagle alpha modification (αMEM) medium (Invitrogen) supplemented with 10% FBS (Cellgro, B003L52), L-glutamine (2 mM), and penicillin (50 U/ml)/streptomycin (50 µg/ml), and split at 1:4 every 3-4 days as needed to avoid over-confluence. For lymphoid differentiation assays, 500 cells were directly sorted into individual wells of a 24-well plate containing 10,000 OP9 stromal cells in OptiMEM medium (Invitrogen) supplemented with 5% FBS (StemCell Technology), L-glutamine (2 mM), penicillin (50 U/ml)/streptomycin (50 µg/ml), 2-mercaptoethanol (50 µM), SCF (10 ng/ml), Flt3L (10 ng/ml), and IL-7 (5 ng/ml). Following sequential withdrawal of Flt3L and SCF upon 2-day intervals, cultures were maintained in IL-7 and analyzed by flow cytometry at various intervals. For CFSE analyses, 1,000-1,500 cells were directly sorted into individual wells of a 96-well plate containing staining media, washed with PBS, resuspended in 100 µl PBS containing 5 µM CFSE (Molecular Probes, C-1157), incubated for 5 minutes at RT, quenched with FBS, incubated for 1 min at RT, washed twice with staining media, resuspended in 200 µl full cytokine medium, incubated for 72 hr and analyzed by flow cytometry. Stromal cells were grown in αMEM supplemented with 10% FBS (CellGro), penicillin (50 U/ml)/streptomycin (50 µg/ml), and 2-mercaptoethanol (50 µM). For fibroblastic colony-forming unit (CFU-F) assays, endosteal MSC-S (15-300 cells) or OLC (170-300 cells) were sorted directly in 6-well plates containing 1.5 ml medium/well and cultured for 11 days with medium exchange every 2-3 days, before staining with Giemsa-Wright to score colonies of 25 or more cells. In contrast, marrow MSC-L (100-300 cells) were sorted directly into 6-well plates containing 1.5 ml

of Dulbecco's Modified Eagle Medium (Gibco) supplemented with 20% FBS (CellGro), penicillin (50 U/ml)/streptomycin (50 µg/ml), 2-mercaptoethanol (50 µM), and 10 µM ROCK inhibitor (TOCRIS, Y-27632) and cultured in hypoxic conditions (5% O₂) for 8 days with medium exchange every 2-3 days, before staining with Giemsa-Wright to score colonies of 25 or more cells. For co-culture assays, 25 β-actin-GFP MSC-S cells were directly sorted into 96-well plates containing 100 µl medium/well, then 1x10⁵ unfractionated BM cells in 100 µl medium were added and co-cultures were incubated for 10 days without medium replacement. On day 10, medium was aspirated and adherent cells were washed twice with PBS, liberated with 50 µl 0.25% trypsin/EDTA (Thermo, 25200056), and counted by flow cytometry using 25 µl Absolute Counting Beads (Life Technologies, C36950). For SA-β-Gal (Cell Signaling, 9860S) staining, MSC-S and OLC were sorted directly onto poly-L-lysine coated slides (Sigma, P0425) and stained according to manufacturer's protocol. For assessing Caspase 1 activity, analysis was performed using the FAM-FLICA Caspase-1 (YVAD) Assay Kit (ImmunoChemistry Technologies, 97) according to manufacturer's instructions.

Bone analyses

Bones for hematoxylin/eosin (H&E) staining were processed by the Mouse Pathology Core Facility at UCSF or the Molecular Pathology Core Facility at CUIMC. Bones for MicroCT analyses were fixed in 10% neutral buffered formalin for 24 hours, then held in 70% ethanol at 4°C until further processing. CT scans were performed on a vivaCT40 MicroCT (Scanco; 55 kV x-ray energy, 10.0 µm voxels, 500 ms integration times) and bone densitometry analyses were performed as previously described (Schepers et al., 2013). Trabecular tissue volume (TV), mineralized bone volume (BV), and trabecular bone parameters were determined on 100 slices, starting 500 µm below the bottom edge of the growth plate using segmentation values of 0.5/2/350 which corresponds to 650 mg hydroxyapatite/cm³.

Immunofluorescence staining

For whole mount imaging, mice were injected retro-orbitally under isoflurane anesthesia with 100 µl of CD31-A647 (BioLegend, 102416) and VE-Cadherin-A647 (BioLegend, 138006) antibody cocktail in PBS. Injected mice were euthanized 10 min later, perfused with 3 ml PBS and fixed by perfusion of 10 ml 4% paraformaldehyde (PFA) in PBS. Femurs were harvested, fixed in 4% PFA for 2 hr on ice, washed 3x with PBS for 10 min each, and then cleared by successive dehydration with sucrose (15% and then 30%) for either 1 hr or overnight at each step. Bones were then snap-frozen in a 100% ethanol/dry ice slurry, and kept at -80 °C until sectioning. One side of the frozen femur was cryosectioned with a tungsten blade (Leica, CM3050 S) until the BM was exposed, then transferred to a 1.5mL Eppendorf tube, washed 3x with PBS at RT and blocked with 20% goat-serum in PBS/0.1% Tween-20 (PBST) overnight at 4°C. Bones were incubated with rabbit anti-mouse laminin (Sigma, L9393) in 10% goat-serum in PBST for 3 days at 4°C, then washed 3x with PBST and incubated with donkey goat anti-rabbit A594 (Thermo Fisher, A32740) for 2 days at 4°C. Finally, bones were washed 3x with PBST for 10 min each, mounted on a cover-slip with silicone glue, kept wet with PBS at all times, and imaged on an SP8 inverted confocal microscope (Leica) with 20x objective. For BM section imaging, mouse femurs were embedded in OCT,

snap-frozen in a 100% ethanol/dry ice slurry, and kept at -80 °C until sectioning. Thin 7 µm section were obtained upon cryosection using the CryoJane tape transfer system (Leica, 39475205) and a tungsten blade. Sections were dried for 2-4 hr at room temperature and then frozen at -80 °C until stained. Before staining, sections were fixed with 100% acetone for 10 min at -20 °C, dried for 5 min at RT, blocked for 90 min with 10% goat-serum (Gibco) in PBS and washes 3x with PBS. For LepR staining, sections were first stained with LepR-biotin (R&D systems, AF497) and rabbit anti-mouse laminin, and then with SA-A555 (ThermoFisher, S21381) and goat anti-rabbit A594 (Thermo Fisher, A32740) followed by blocking with rat IgG for 10 min at RT. Slides were then stained with A488-conjugated lineage markers Ter119 (BioLegend, 116215), Mac-1 (BioLegend, 101217), Gr-1 (BioLegend, 108417), B220 (BioLegend, 103225), CD41 (Thermo Fisher, 11-0411-82) and CD3 (BioLegend, 100210). For ALCAM staining, sections were first stained with anti-ALCAM-Bio (R&D systems, BAF1172) followed by SA-A555 blocked with rat IgG and then stained with A488-conjugated lineage markers. For laminin staining, sections were stained with rabbit anti-mouse laminin followed by goat anti-rabbit-A647 and, eventually, DGB fluorescence was detected in the A488 channel. For GMP staining, sections were first stained with rat anti-mouse c-Kit (BioLegend, 135102) followed with a goat anti-rat-Cy3 (Jackson ImmunoResearch, 112-165-167), and then with A488-conjugated lineage markers, Sca-1-A488 (BioLegend, 108116), CD150-A488 (BioLegend, 115916) and FcyR-A647 (BioLegend, 101314). After staining, all sections were counterstained with 1 µg/ml DAPI in PBS for 10 min at RT, mounted with Fluoromount G (Southern Biotech, 0100-01) and imaged on an SP5 upright confocal microscopes (Leica) with 20x objectives. For DGB staining of purified SECs, 2,000 cells were sorted directly onto poly-L-lysine coated slides (Sigma-Aldrich, P0425-72EA) and allowed to settle for 10 min before being fixed with 4% PFA for 10 min at RT, washed and counterstained with 1 µg/ml DAPI in PBS for 10 min at RT, mounted with VectaShield (Vector Laboratories, H-1200) and imaged on an A1 Ti Eclipse inverted microscope (Nikon) with 20x objectives. Images were processed using Volocity software (Perkin Elmer v.6.2) and analyzed with ImageJ. The find objects function in Volocity was used to quantify vascular volume based on Laminin staining.

Cytokine profiling

For each individual mouse, BM fluid was flushed out from the four hind leg bones (two femurs and two tibiae) using the same 200 µl of HBSS/2% FBS in a 1 ml syringe with 26G needle. BM cells were sedimented by centrifugation at 300 g for 5 min and collected supernatants were purified by an additional centrifugation at 15,300 g for 10 min. BM fluids were stored at -80°C until use. For 200-plex cytokine array, BM fluid samples were submitted to Quantibody Testing Service (Raybiotech) and diluted 4x prior to analyses. For bead array analysis, 50 µl of 2x diluted sample was analyzed using Mouse 20-Plex panel (Thermo Fischer Scientific) using either a Magpix (UCSF) or Luminex 200 (CUIMC) analyzer according to manufacturer's protocol. For ELISA measurements, 4x-diluted (SCF, SDF1a, TPO; Raybiotech) and 90x-diluted (TGF-β; R&D Systems) samples were prepared according to the manufacturer's instructions and analyzed on a Synergy 2 plate reader (Biotek).

Plate-based scRNAseq

Samples were processed following modifications to the Smart-Seq2 protocol (Picelli et al., 2014) based in the mcSCRB-Seq protocol (Bagnoli et al., 2018). Single endosteal and central marrow stromal cells were directly sorted into individual wells of a 96-well PCR plate in 2.3 μ l of lysis buffer containing 0.2% Triton X-100 (Sigma-Aldrich) and 1U of Superase-In RNase Inhibitor (Ambion). Of note, information regarding expression of surface markers was recorded for each cell when sorting. Cells were frozen immediately at -80C until further processing. After thawing on ice, 2 μ l of an annealing mixture containing 1 μ M oligodT (IDT), 5 mM each dNTPs and a 1:6,000,000 dilution of ERCC RNA Spike-In Mix (Invitrogen) was added followed by incubation at 72 °C for 3 min. Then 5.7 μ l of a Reverse Transcription mix containing 3.5 U/ μ l of Maxima H minus retrotranscriptase (ThermoFisher), 0.88 U/ μ l of Superase-In RNase Inhibitor, 1.75x Maxima RT Buffer, 3.5 μ M TSO (Qiagen) and 13.15% PEG 8000 (Sigma-Aldrich) was added and the mixture was incubated at 42 °C for 90 min, followed by 70 °C for 15 min. cDNA was further amplified by adding 40 μ l of a PCR mix containing 0.03 U/ μ l of Terra PCR direct polymerase (Takara Bio), 1.25x Terra PCR Direct Buffer, and 0.25 μ M IS PCR primer (ID). PCR was as follows: 3 min at 98 °C for initial denaturation followed by 21 cycles of 15 s at 98 °C, 30 s at 65 °C, 4 min at 68 °C. Final elongation was performed for 10 min at 72 °C. Sequences of oligodT, TSO and IS PCR primers were as previously described (Picelli et al., 2014). Following preamplification, all samples were purified using Ampure XP beads (Beckman Coulter) at a ratio of 1:0.6 with a final elution in 25 μ l of EB Buffer (Qiagen). The cDNA was then quantified using the Quant-iT PicoGreen dsDNA Assay Kit (Thermo Fisher). Size distributions were checked on high-sensitivity DNA chips (Agilent Bioanalyzer). Samples were used to construct Nextera XT libraries (Illumina) from 100 pg of preamplified cDNA. Libraries were purified and size selected (0.5x-0.7x) using Ampure XP beads. Then, libraries were quantified using KAPA qPCR quantification kit (KAPA Biosystems), pooled and sequenced in an Illumina HiSeq 4000 instrument. Reads were mapped to the *Mus musculus* genome (EMSEMBL GRCm38.p4 Release 81) and ERCC sequences using GSNAP (version 2015-09-29) with parameters: -A sam -B 5 -t 24 -n 1 -Q -N 1. HTseq-count (Anders et al., 2015) was used to count reads mapped to each gene, with parameters: -s no. All cells with < 100,000 reads mapping to endogenous RNA and >20% reads mapping to mitochondrial genes were considered low quality and removed from downstream analyses. Overall, 661 cells (67.38%) passed our quality controls distributed as follows: Young marrow EC (SEC), 70; Old marrow EC (SEC), 71; Young endosteal EC (AEC), 84; Old endosteal EC (AEC), 82; Young MSC-L, 53; Old MSC-L, 58; Young MSC-S, 59; Old MSC-S, 59; Young mOPr, 26; Old mOPr, 26; Young OPr, 44; Old OPr, 29. The mean of nuclear reads mapped per cell was 471,244. Data were normalized and highly variable genes were identified as previously described (Brennecke et al., 2013), using a false discovery rate threshold equal to 0.1 for the chi-squared test. Only highly variable genes were considered to perform PCA analysis, using the *prcomp* function in R (version 3.6.3). UMAP was calculated using *umap* function (version 0.2.7) in R based on normalized expression value with 15 nearest neighbors. All genes were used for ICGS clustering (AltAnalyzer) (Olsson et al., 2016) of mesenchymal and endothelial populations. In both cases we used version (v2.0) and 'stringent' with cell cycle and all other parameters as default. For mesenchymal populations, 16 clusters of cells (denoted M1 to M16) and 6 clusters of genes (denoted A to F) were defined. For endothelial populations, 7 clusters of cells (denoted E1 to E7) and 6 clusters of genes (denoted a to g) were defined. For subsequent analysis, mesenchymal clusters of cells were pooled as

follows: M1 and M2 for “MSC-L-like”; M3, M4 and M5 for “OPr-like”; M6 to M16 for “MSC-S-like”. Subsequent endothelial groups of cells were defined as follows: clusters E3 and E4 constituted “AEC-like”; cluster E7 “SEC-like”. For MSC-L gene identity comparison, the geometric mean of the expression of all genes contained in cluster A was calculated for each cell of clusters M1 and M2 and then clusters M1 and M2 were compared using the independent two-sided t test (p -value $< 2.2e-16$). Differential expression analysis of old and young cells within each group was performed using DESeq2 (Love et al., 2014) version 1.26.0. For violin plots representation, normalized expression values of *Kitl*, *Cxcl12*, *Il1a*, *Il1b* and *Il1rn* were plotted in various groups for young and old cells using the *ggplot2* package (version 3.3.0) in R with scale parameter set to ‘width’. Pathway analysis was conducted using Gene Set Enrichment Analysis (GSEA) software v4.1.0. Gene symbols were mapped to MSigDB.v7.2.chip and overlaps with Hallmark (h.all.v7.2.symbols.gmt) gene sets were determined using the classic scoring scheme. For endothelial cell types, no $FDR < 0.05$ significant enrichments were obtained using GSEA, and so Ingenuity Pathway Analyses software (Qiagen, December 2020) was eventually employed. For IPA of endothelial cells, log 2 fold change of expression and p -adjusted values for all genes with nominal p values under 0.05 were imported into the software and IPA Canonical Pathways were determined.

Droplet-based scRNAseq for stroma analyses

For both endosteal and central marrow populations, 30,000-50,000 Ter119⁻/CD45⁻ stromal cells were sorted into 1.5 ml tubes containing 500 μ l of filter-sterilized α MEM with 10% FBS and transferred to the Columbia Genome Center Single Cell Analysis Core for microfluidic cell processing, library preparation and sequencing. In brief, cells were re-counted and viability was assessed using a Countess II FL Automated Cell Counter (Thermo), and samples were processed following manufacturer’s recommendations for Chromium Single Cell 3’ Library & Gel Bead Kit v2 (10X Genomics). 17,500 cells were loaded for each sample and 1 sample was loaded per condition. Samples were sequenced in Illumina HiSeq4000 sequencer machine. We obtained an average of ~286 million reads per sample. The alignment was done using *Cellranger* (version 2.1.1). Top 2,300 barcodes were selected for samples corresponding to young and old central marrow and young endosteum. Top 2,858 barcodes were selected for the sample corresponding to old endosteum. The downstream analysis was done using *Scanpy* version 1.6.0 (Wolf et al., 2018) in *Python* version 3.7.1. For these samples, 757 doublets were estimated and removed using *Scrublet* package version 0.2.1 (Wolock et al., 2019). Further quality control (QC) was performed based on 3 parameters: 1) cells with at least 200 and no more than 7,000 genes detected; 2) cells with less than 65,000 associated counts; 3) cells with less than 5.5% of UMI counts associated to mitochondrial genes. After QC, 8,735 cells were kept for subsequent analysis. In addition, only genes that have more than 1 UMI count in at least 5 cells were maintained in further analysis. Cells were then normalized to 10,000 UMIs per cell and logarithmically transformed. Highly variable genes (HVGs) were selected using “highly_variable_genes” method with “min_mean=0.0175, max_mean=3, min_disp=0.5”. Read depth, number of genes and number of mitochondrial counts were removed using the “regress_out” function in *Scanpy*. UMAP visualizations were obtained from 50 PCA components and 10 neighbors using *Scanpy*. Clusters were defined using *Louvain* clustering version 0.7.0. Clusters containing stromal

cells were subset based on the expression of genes expressed mainly in either hematopoietic cells or stromal cells. Only clusters that contained cells that expressed stromal marker genes were kept for subsequent analysis. In total, 2378 cells were selected, distributed as follows: 188 cells came from the young central marrow sample, 726 cells from the old central marrow sample; 1320 cells came from the young endosteum sample and 144 cells from the old endosteum sample. Highly variable genes (HVGs) were then obtained for the selected cells and the effects of read depth, number of genes and number of mitochondrial counts were regressed, as indicated above. The UMAP visualization was obtained as before and again clusters were defined using Louvain clustering with “*resolution 0.3*”. Cell types were annotated using typical marker genes for the different populations.

Droplet-based scRNAseq for hematopoietic analyses

For both LK and LSK populations, 30,000-50,000 cells were sorted into 1.5 ml tubes containing 500 µl of HBSS containing 2% FBS and transferred to the Columbia Genome Center Single Cell Analysis Core for microfluidic cell processing, library preparation and sequencing as described above for stromal analyses. Downstream analyses done using *Seurat* version 4.0.3 in *R* version 4.1.0. Quality control (QC) was performed excluding cells with less than 200 genes detected or more than 7.5% of UMI counts associated to mitochondrial genes. In addition, only genes that have more than 1 UMI count in at least 3 cells were maintained in further analysis. In total, 28535 cells were selected, distributed as follows: 8489 cells came from the young WT sample, 9688 cells from the old WT sample; 10358 cells came from the old *//1r1^{-/-}* sample. Cells were then normalized to 10,000 UMIs per cell and logarithmically transformed. Highly variable genes (HVGs) were selected using the “FindVariableFeatures” method. Cell cycle variation was removed using the “CellCycleScoring” method followed by regressing out “S.Score” and “G2M.Score”. Young WT and Old WT samples were integrated using the “IntegrateData” method (Stuart et al., 2019). UMAP visualizations were obtained from 10 PCA components and clusters were defined at a resolution of 0.4 using K-nearest neighbor graph-based. Cell types were annotated using typical marker genes for the different hematopoietic populations. Differential gene expression was performed using “FindMarkers” method on non-cell cycle regressed expression data. Old *//1r1^{-/-}* data was analyzed by mapping to the Young WT/Old WT reference dataset using the “MapQuery” method (Hao et al., 2021).

Quantitative RT-PCR analyses

10,000-50,000 cells per population were sorted directly into RPE buffer (Qiagen) and stored at -80°C until purification with the RNeasy Plus Mini Kit (Qiagen) according to manufacturer’s protocol. Following column purification, RNA was immediately reverse-transcribed using SuperScriptIII kit with random hexamers (Invitrogen). qPCR runs were performed on a QuantStudio 7 Flex Real-Time PCR System (Applied Biosystems) using SYBR Green reagents (Applied Biosystems), the cDNA equivalent of 200 cells per reaction template, and triplicate measurement per biological repeat. Sequences for qRT-PCR primers were: *//1a*, forward GCACCTTACACCTACCAGAGT and reverse TGCAGGTCATTTAACCAAGTGG (NM_010554); *//1b*, forward GCAACTGTTCTGAACTCAACT and reverse ATCTTTTGGGGTCCGTCAACT (NM_008361); *Tnf*, forward AGGGATGAGAAGTTCCCAAAT and reverse GCTTGCTACTCGAATTTTGGAG

(NM_013693); and *Gapdh*, forward GACTTCAACAGCAACTCCCAC and reverse TCCACCACCCTGTTGCTGTA (NM_008084). Cycle threshold values were normalized to *Gapdh*.

Fluidigm analyses

Gene expression analyses using the Fluidigm 96.96 Dynamic Array IFC were performed as previously described (Pietras et al., 2015). Briefly, HSC, MPP3 and MPP4 (100 cells/well) were directly sorted per well of a 96-well plates containing 5 μ l CellsDirect lysis buffer (Invitrogen, 11753-100), reverse-transcribed and pre-amplified for 18 cycles using SuperScript III Platinum Taq Mix (Invitrogen, 12574-026) with a custom-made set of 96 proprietary target-specific primers (Fluidigm). The resulting cDNA was analyzed on a Biomark system (Fluidigm) using EvaGreen SYBR dye (Bio-Rad, 172-5211). Data were collected with Biomark Data Collection Software (Fluidigm) and analyzed using Biomark qPCR software with a quality threshold of 0.65 and linear baseline correction. Melt curves and melting temperature values for each assay reaction were checked individually, and reactions with melt curves showing multiple peaks or poor quality were discarded. Results for 2 and 3 weeks post-transplantation data were recalculated with *Hprt* as housekeeping gene and genes not analyzed in one of three conditions were removed, leaving 64-68 genes excluding housekeeping genes (*Actb*, *Gapdh*, *Gusb* and *Hprt*) for further analyses and calculation of Pearson's correlation coefficients. For each dataset, values for each gene were averaged, and fold change values were calculated against young non-transplanted control and converted to Log₂ value. Similarity matrixes were visualized with *Morpheus* (Broad Institute).

Microarray analyses

Microarray analyses of old HSCs, MPP3 and MPP4 were performed as previously described (Pietras et al., 2015). Three to five independent biological replicates were used for each population. Total RNA was isolated from 20,000 cells per population sorted directly into TRIzol-LS (Invitrogen) and purified using Arcturus PicoPure (Applied Biosystems) with RNase-free DNase (Qiagen). RNA was amplified, labeled, and fragmented using NuGEN Ovation Pico linear amplification kits (Nugen Technologies) and hybridized onto mouse Gene ST 1.0 arrays (Affymetrix). Gene expression microarray data were normalized using RMA followed by quantile normalization as implemented in the 2.15.1 R package (www.r-project.org) using a standard ($\lambda=1$) exponential reference distribution. Significance Analysis of Microarrays (SAM) (Tusher et al., 2001) was then performed on young and old cells within a population to determine SAM delta scores. Pathway analysis was performed using GSEA version 4.1.0 on the top 1000 up and downregulated genes in young versus old for each population. Gene symbols were mapped to MSigDB.v7.2.chip and overlaps with Reactome (c2.cp.reactome.v7.2.symbols.gmt) gene sets were determined using the classic scoring scheme.

Quantitation and Statistical Analysis

All experiments were repeated as indicated; n indicates the numbers of independent biological repeats. Data are expressed as mean \pm standard deviation (S.D.) or standard error of the mean (S.E.M.) as indicated. Mice for treatment and transplantation were randomized, samples were alternated whenever

possible, and no blinding protocol was used. No statistical method was used to predetermine sample size. Pairwise statistical significance was evaluated by two-tailed Student's t-test. P-values (p) ≤ 0.05 were considered statistically significant. For violin plot analyses of scRNAseq data, p-values for each comparison were obtained by two-tailed Student's t-test and adjusted for multiple comparisons using the Benjamini-Hochberg method. Adjusted p-values (p_{adj}) ≤ 0.05 were considered statistically significant. Figures were made with GraphPad Prism software.

Data and Software Availability

Data sets that support the findings of this study have been deposited in the Gene Expression Omnibus (GSE169162). Source data for all the figures are provided with the paper. All other data are available from the corresponding author upon reasonable request.

Figures

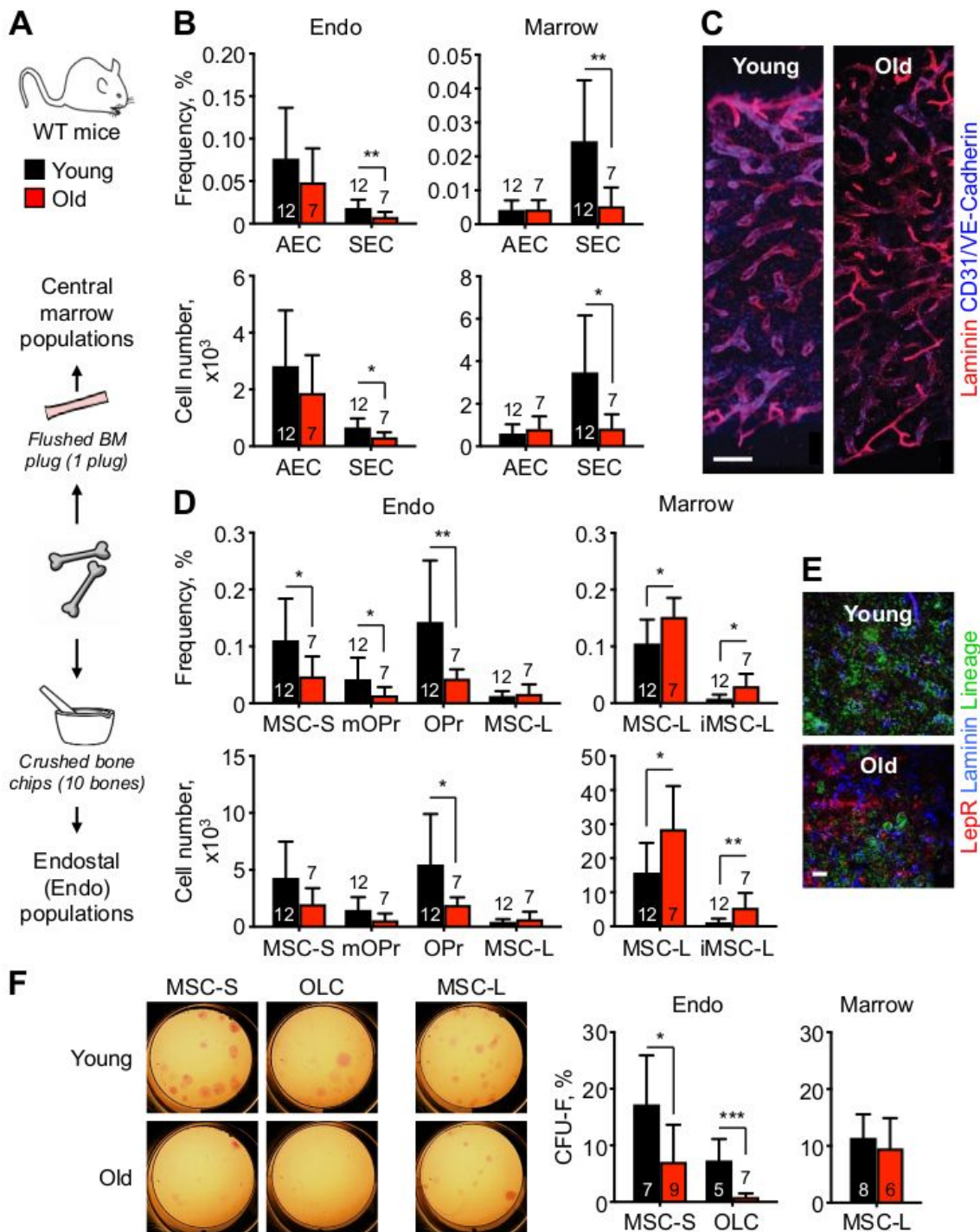


Figure 1

Figure 1

Remodeled BM microenvironment with age. (A) Experimental scheme to investigate endosteal (Endo) and central marrow (Marrow) stromal populations in young (~ 8 week of age) and old (~ 24 months of age) C57BL/6 wild type (WT) mice. Results are from 6 independently analyzed groups of 1 or 2 young or old mice. Cellularity data per mouse are for 1 BM plug for marrow populations and bone chips from 10 bones for endosteal populations. (B) Changes in endosteal and marrow endothelial cell (EC) populations with

age showing frequency (top) and total cell numbers (bottom). AEC, arteriolar endothelial cell; SEC, sinusoidal endothelial cell. (C) Whole mount staining of the BM vasculature in young and old mice. Scale bar, 100 μ m. (D) Changes in endosteal and marrow mesenchymal populations with age showing frequency (top) and total cell numbers (bottom). MSC, Sca-1+ peri-arteriolar mesenchymal stroma cell; mOPr, PDGFR α + multipotent osteoprogenitor; OPr, PDGFR α - osteoprogenitor; MSC-L, LepR+ peri-sinusoidal mesenchymal stroma cell; iMSC-L, Sca-1^{low} inflammatory MSC-L. (E) Representative image of MSC-L immunofluorescence staining in young and old BM. Scale bar, 38 μ m. (F) Representative pictures and quantification of fibroblast colony-forming units (CFU-F) from young and old MSC-S, osteoblastic lineage cell (OLC) and MSC-L. Results are from 5 independent cohorts. Data are means \pm S.D.; * $p \leq 0.05$, ** $p \leq 0.01$, *** $p \leq 0.001$. See also Figure S1.

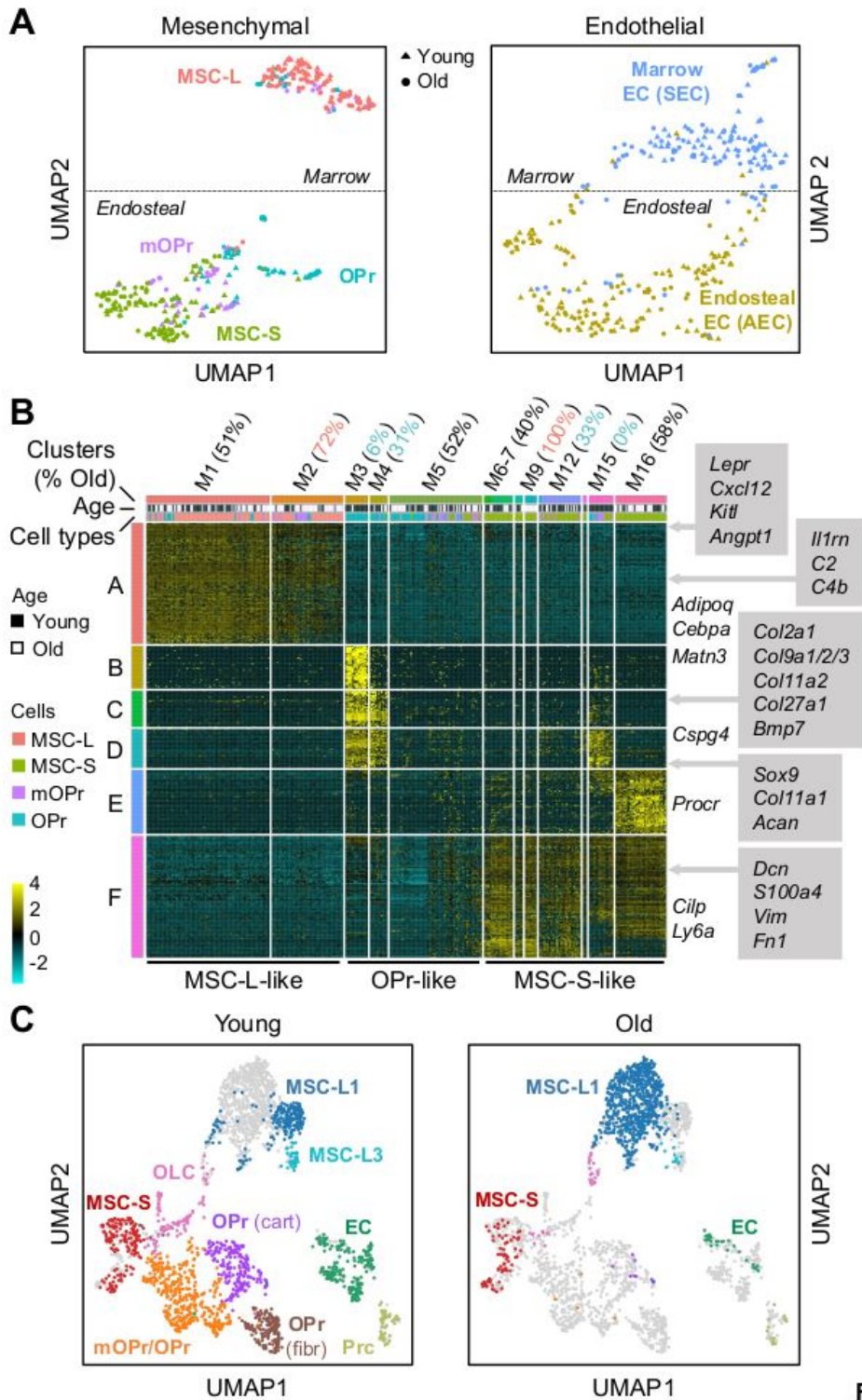


Figure 2

Figure 2

Molecular characterization of the old BM niche. (A) UMAP visualization of plate-based scRNAseq analyses of mesenchymal (left) and endothelial (right) populations isolated from young ($n = 3$) and old ($n = 4$) mice. (B) ICGS output of young and old mesenchymal populations with 16 clusters of cells (M1 to M16, horizontal) defined according to the expressing pattern of the 6 clusters of genes (A to F, vertical). Examples included in gene clusters A to F are shown. (C) UMAP visualization of droplet-based scRNAseq

analyses of endosteal and central marrow stroma fractions isolated from young (n = 2) and old (n = 1) mice. OLC, osteolineage cell; OPr(cart), cartilagenic osteoprogenitor; OPr(fibr), fibrogenic osteoprogenitor; Prc, pericyte. See also Figure S2, Figure S3, Table S1 and Table S2.

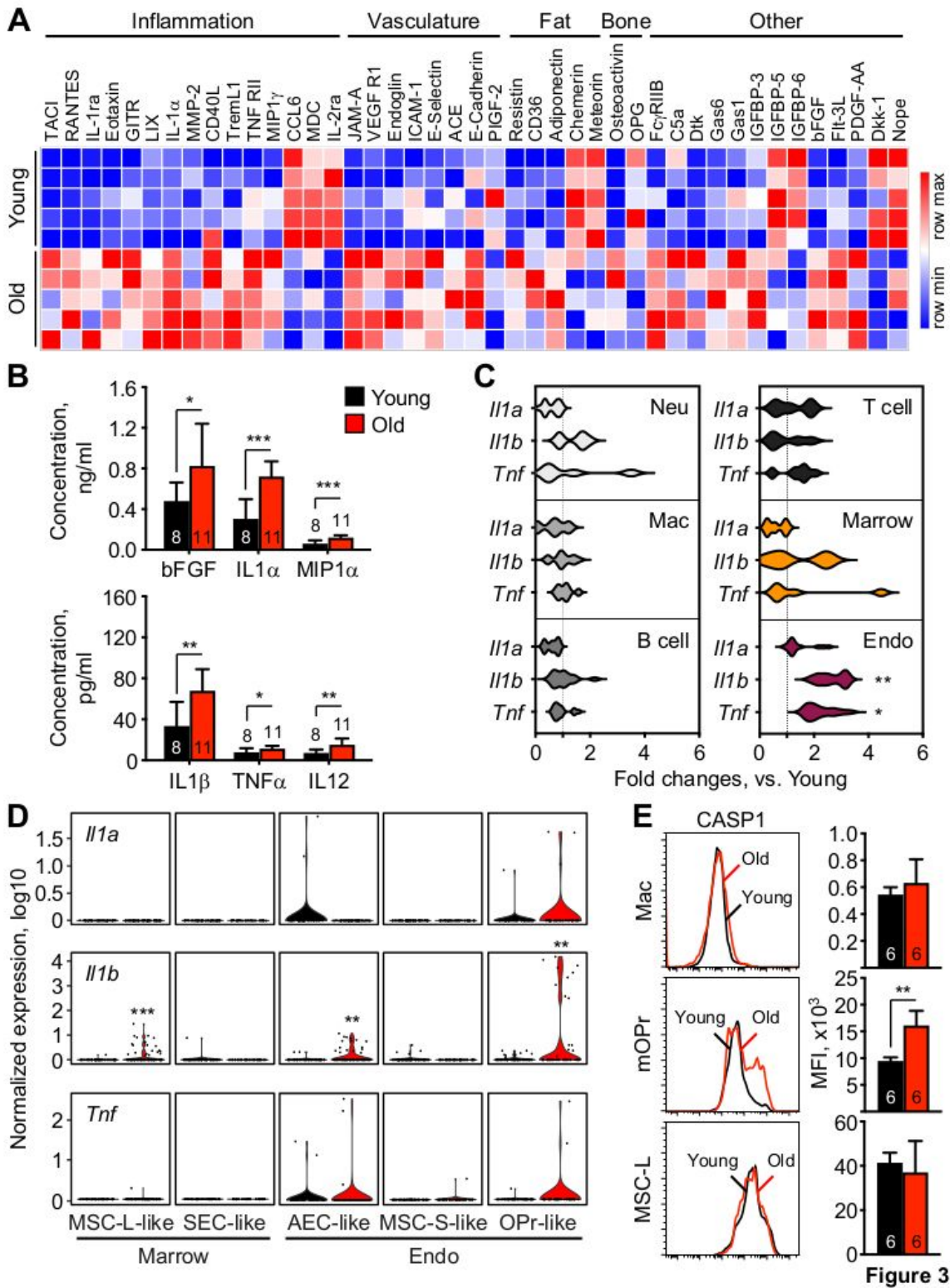


Figure 3

Inflammatory nature of the old BM niche. (A) Differentially secreted cytokines in young and old BM fluid measured by 200-plex array and clustered based on broad biological functions (n = 5). (B) Changes in

pro-inflammatory cytokines in young and old BM fluids. Results are from 3 independent cohorts. (C) qRT-PCR-based analyses of Il1a, Il1b and Tnf expression in old BM cells and stromal fractions (n = 6). Results are represented as violin plots and are expressed as fold change compared to their respective young counterpart; *p ≤ 0.05. Neu, Mac-1+/Ly-6G+/Ly-6Cmid neutrophil; Mac, Mac-1+/Ly-6G-/Ly-6C- macrophage; B cell, B220+/CD19+ B cell; T cell, CD4+/TCRβ+ T cell; Marrow, Ter119-/CD45- central marrow fraction; Endo, Ter119-/CD45- endosteal fraction. (D) Violin plots representation of Il1a, Il1b, and Il1rn expression in the indicated young and old mesenchymal and endothelial like groups. Results are from the plate-based scRNAseq dataset; *padj ≤ 0.05, ** padj ≤ 0.01, *** padj ≤ 0.001. (E) Caspase 1 (CASP1) activity in the indicated young and old BM and stromal populations with representative FACS plots (left) and quantification (right). Data are means ± S.D.; *p ≤ 0.05, **p ≤ 0.01, ***p ≤ 0.001. See also Figure S4 and Table S3

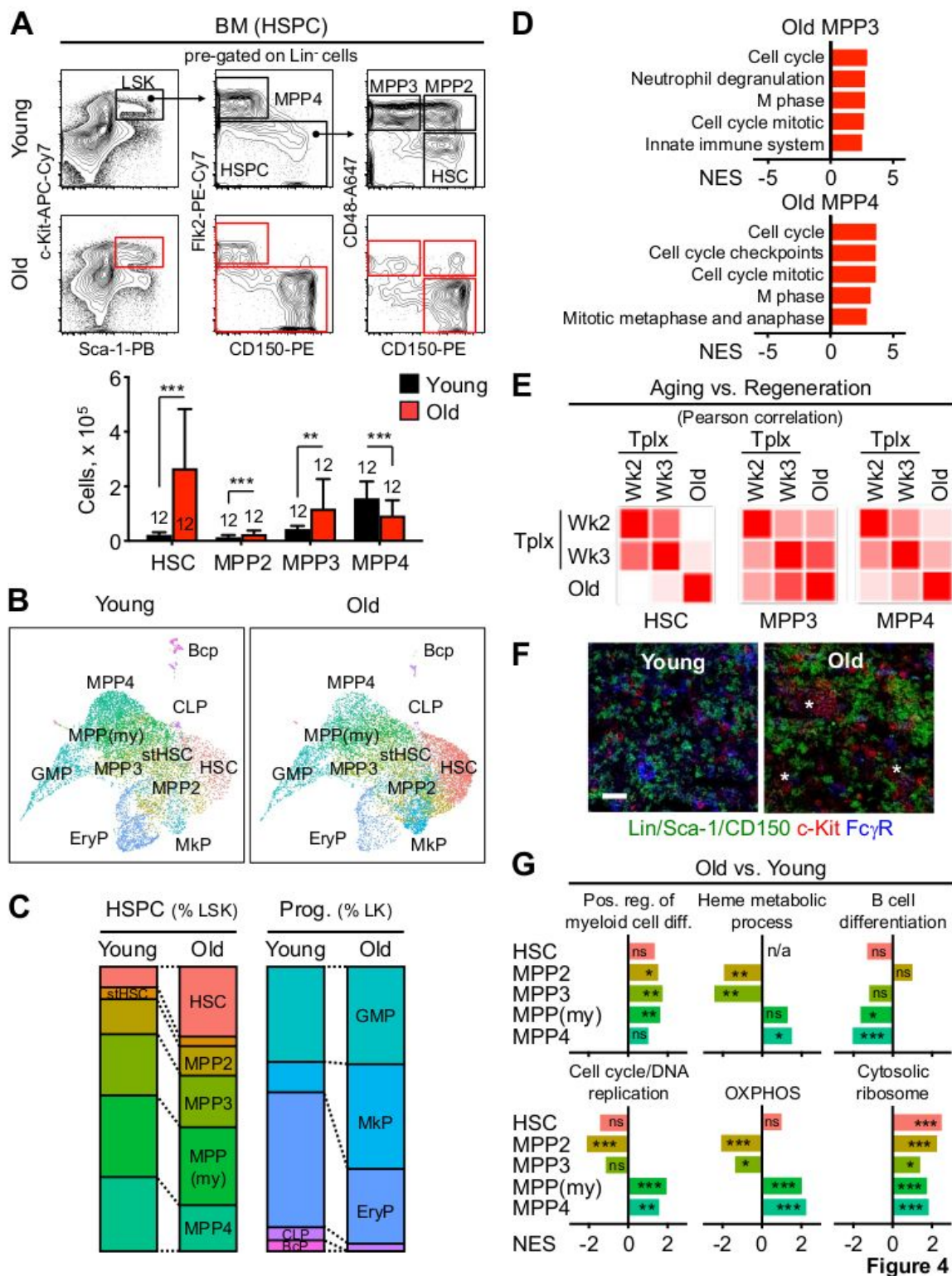


Figure 4

Activation of emergency myelopoiesis pathways in the old blood system. (A) Representative flow cytometry plots (top) and quantification (bottom) of HSCs and MPP populations in young and old mice. Results are from 4 independent cohorts with data expressed are means \pm S.D.; ** $p \leq 0.01$, *** $p \leq 0.001$. (B) UMAP visualization of droplet-based scRNAseq analyses of Lin⁻/c-Kit⁺ (LK) and Lin⁻/Sca-1⁺/c-Kit⁺ (LSK) BM fractions isolated from young ($n = 2$) and old ($n = 1$) mice. stHSC, short-term HSC; MPP(my),

myeloid-primed MPP; GMP, granulocyte/macrophage progenitor; EryP, erythroid progenitor; MkP, megakaryocyte progenitor; CLP, common lymphoid progenitor; BcP, B cell progenitor. (C) Quantification of the HSPCs and progenitors (Prog.) identified by droplet-based scRNAseq analyses. Results are expressed as percent LSK and LK, respectively. (D) GSEA results for Reactome pathway analyses of isolated young and old MPP3 and MPP4 analyzed by microarray (FDR < 0.05; n = 3 per population). (E) Pearson correlation of Fluidigm gene expression data comparing old and regenerative HSCs, MPP3 and MPP4 (n = 4 per population). Regenerating populations were isolated 2 and 3 weeks following young HSC transplantation (Tplx) (Pietras et al., 2015). (F) Representative image of GMP immunofluorescence staining in young and old BM. Stars indicate self-renewing GMP patches. Scale bar, 60 μ m. (G) GSEA results for Gene Ontology analyses of affected pathways in old populations identified by droplet-based scRNAseq analyses. n/a, non-available; ns, non-significant; *nominal p value \leq 0.05, ** nominal p value \leq 0.01, *** nominal p value \leq 0.001. See also Figure S4, Figure S5 and Table S4.

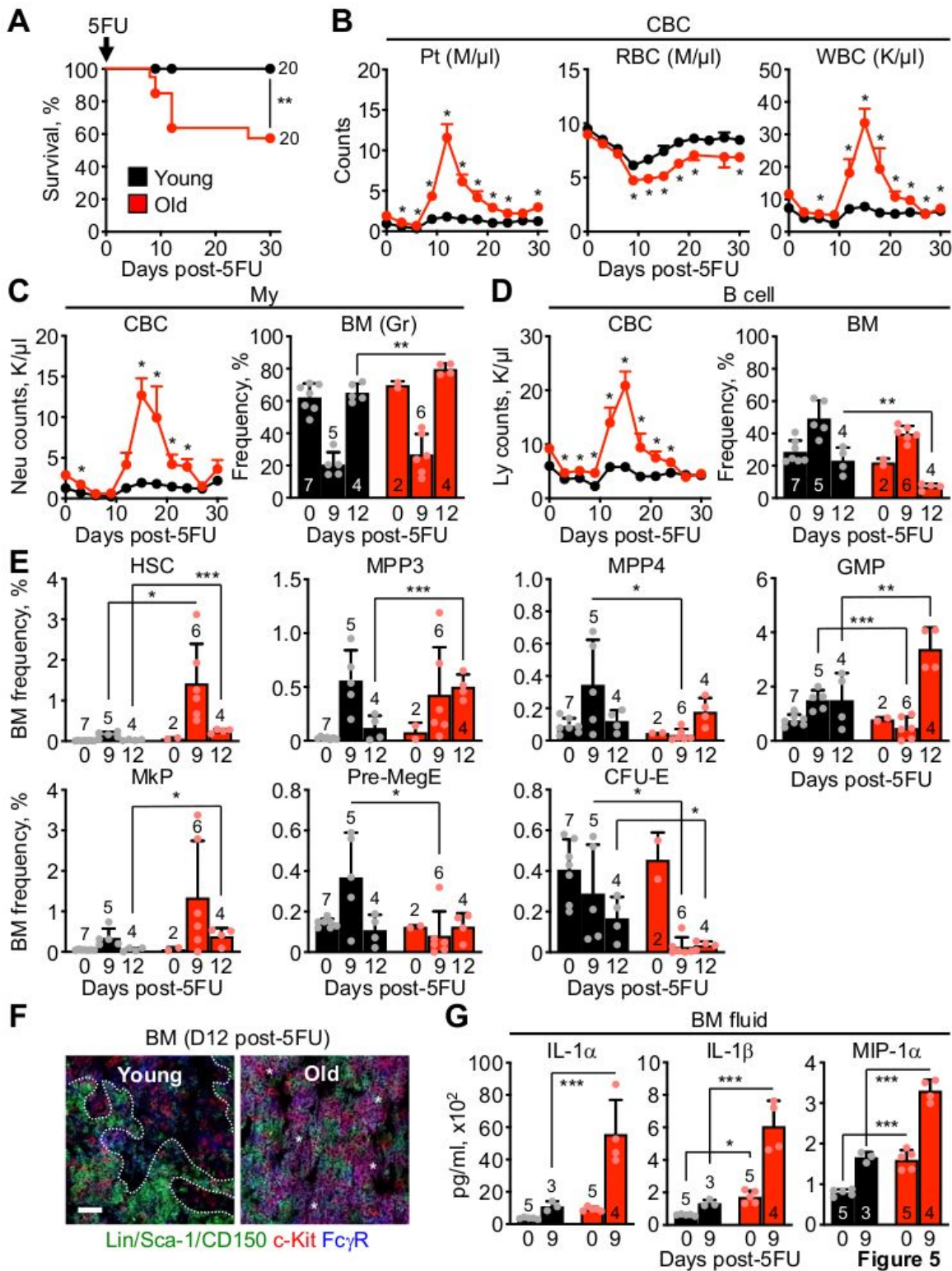


Figure 5

Impaired hematopoietic regeneration in old mice. (A-B) Summary of (A) survival and (B) blood regeneration in young and old mice following one 5FU injection. Results are from 3 independent cohorts started with 20 individual young and old mice injected with 5FU per group. (C-D) Regeneration of (C) myeloid and (D) B cell populations post-5FU treatment of young and old mice with quantification of changes in the blood (left) and BM (right).. (E) Regeneration of the indicated BM progenitor populations

post-5FU treatment of young and old mice. (F) Representative image of GMP immunofluorescence staining at 12 days (D12) post-5FU treatment of young and old mice. Dotted lines indicate differentiating GPM clusters and stars self-renewing GMP patches. Scale bar, 60 μ m. (G) Changes in IL-1 α and IL-1 β levels in BM fluids post-5FU treatment of young and old mice. Data are means \pm S.D. except for CBC data shown in B, C and D (\pm S.E.M.); * $p \leq 0.05$, ** $p \leq 0.01$, *** $p \leq 0.001$.

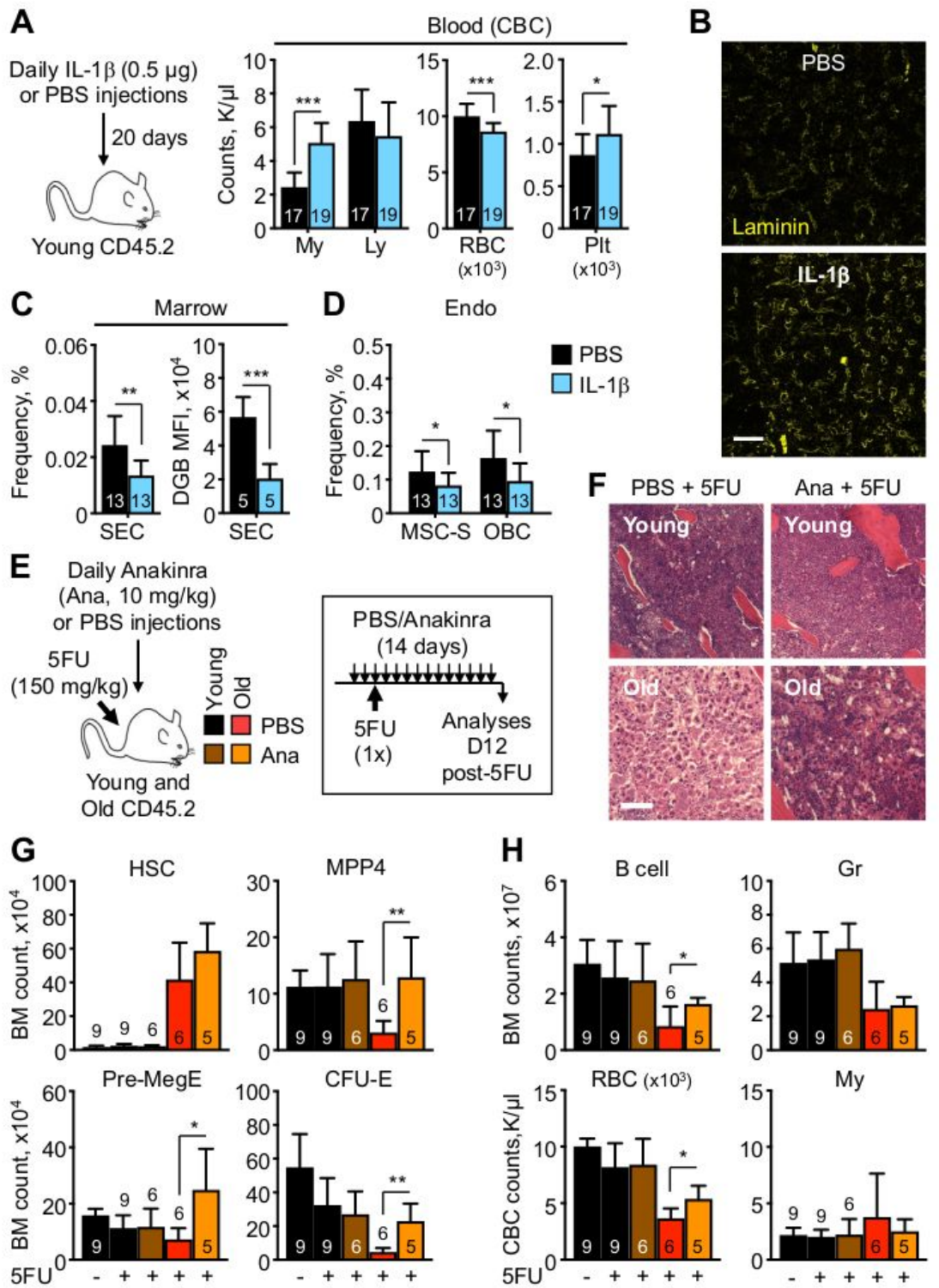


Figure 6

Figure 6

Modulating IL-1 levels in young and old mice affect aging parameters. (A-D) Pro-aging effects of chronic IL-1 β exposure in young mice with: (A) experimental scheme (left) and CBC values (right); (B) representative staining of the BM vasculature (scale bar, 100 μ m); (C) changes in SEC frequency (left) and dragon green beads (DGB) retention (right); and (D) changes in the indicated endosteal mesenchymal populations. Results are from 4 independent cohorts of young and old mice injected daily with either PBS or IL-1 β for 20 days. (E-H) Pro-regenerative effects of acute IL-1 signaling blockade with Anakinra (Ana) in 5FU-treated old mice with: (E) experimental scheme; (F) representative H&E staining of sternum (scale bar, 100 μ m); (G) quantification of the indicated BM HSPCs; and (H) quantification of the indicated BM mature populations and blood parameters. Results are from 3 independent cohorts started with 15 young and 11 old mice treated once with 5FU, injected daily with either PBS or Anakinra, and analyzed at day 12 post-5FU treatment. Data are means \pm S.D.; * $p \leq 0.05$, ** $p \leq 0.01$, *** $p \leq 0.001$. See also Figure S6.

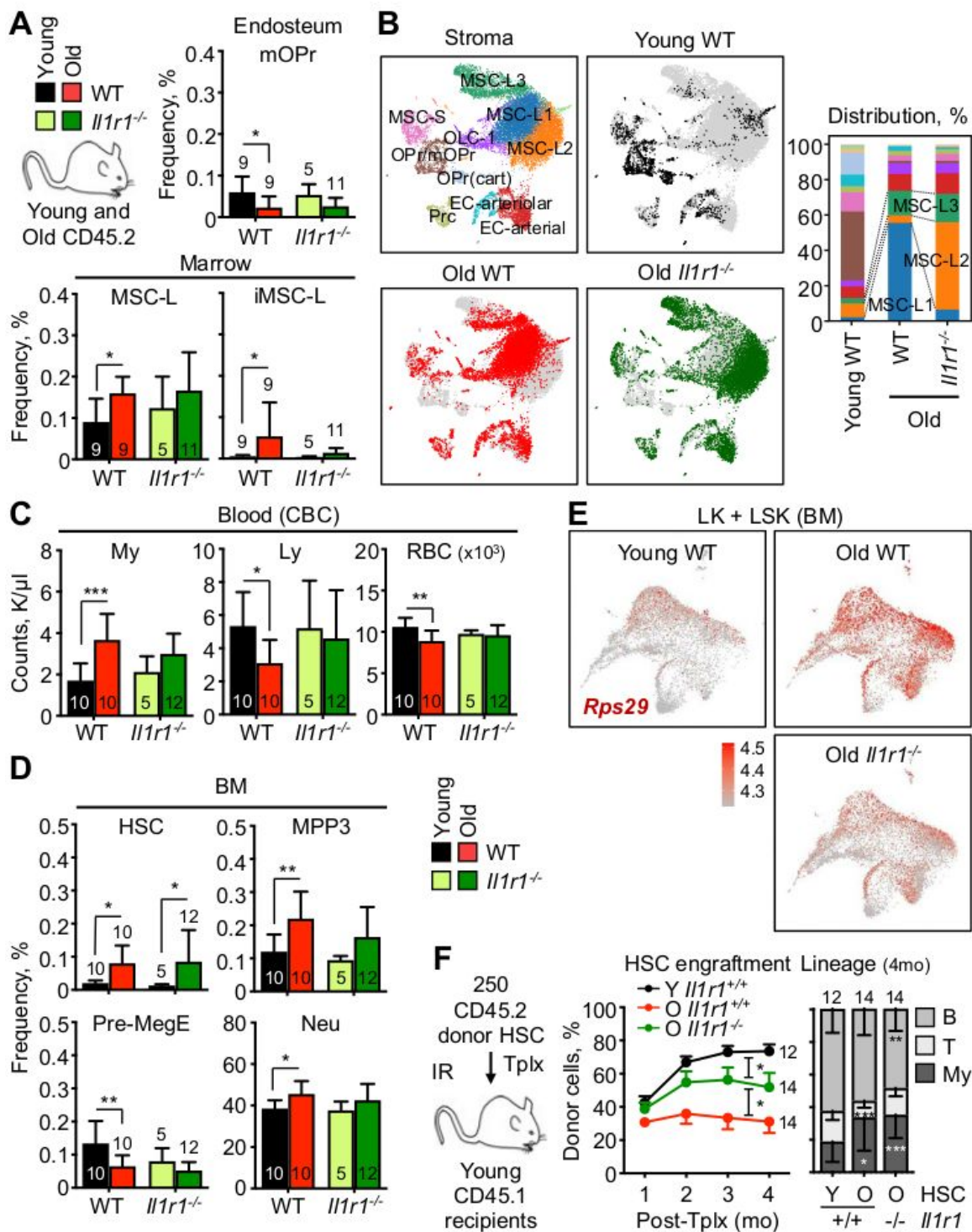


Figure 7

Figure 7

Blocking IL-1 signaling delays niche aging and improves old blood parameters. (A-B) Improved stromal aging features in old *Il1r1*^{-/-} mice with: (A) color scheme (left) as well as endosteal (right) and central marrow (bottom) mesenchymal population frequencies; and (B) UMAP visualization of droplet-based scRNAseq analyses of endosteal and central marrow stromal fractions in young (n = 2) and old (n = 2) *Il1r1*^{+/+} wild type (WT) mice and old (n = 1) *Il1r1*^{-/-} mice with quantification of percent of the different

mesenchymal and endothelial populations (right). (C-F) Delayed blood aging and improved HSC function in old *Il1r1*^{-/-} mice with: (C) blood parameters, (D) BM hematopoietic population frequencies, (E) *Rps29* expression in the droplet-based scRNAseq of old WT/*Il1r1*^{-/-} LK/LSK dataset shown in Figure S7C; and (F) engraftment over time (left) and lineage reconstitution (right) at 4 months (4 mo) post-transplantation (Tplx) of the indicated HSC populations. Results are from 3 independent cohorts of young and old WT and age-matched *Il1r1*^{-/-}, with HSCs isolated from the pooled BM of mice of the same genotype and transplanted into 3 to 5 recipients, each. Data are means \pm S.D. except except for engraftment results shown in F (\pm S.E.M.); * $p \leq 0.05$, ** $p \leq 0.01$, *** $p \leq 0.001$. See also Figures S6 and S7.

Supplementary Files

This is a list of supplementary files associated with this preprint. Click to download.

- [Mitchelletal.TableS1Revised.xlsx](#)
- [Mitchelletal.TableS4Revised.xlsx](#)
- [Mitchelletal.SupplementaryInformationRevised.pdf](#)
- [Mitchelletal.TableS2Revised.xlsx](#)